

# CHEX-MATE: exploring the kinematical properties of Planck galaxy clusters <sup>★</sup>

Lorenzo Pizzuti<sup>1</sup>, Rafael Barrena<sup>2,3</sup>, Mauro Sereno<sup>4,5</sup>, Alina Streblyanska<sup>2,3</sup>, Antonio Ferragamo<sup>6</sup>, Sophie Maurogordato<sup>7</sup>, Alberto Cappi<sup>4,7</sup>, Stefano Ettori<sup>4,5</sup>, Gabriel W. Pratt<sup>8</sup>, Gianluca Castignani<sup>4</sup>, Megan Donahue<sup>9</sup>, Dominique Eckert<sup>4,5</sup>, Fabio Gastaldello<sup>10</sup>, Raphael Gavazzi<sup>11,12</sup>, Christopher P. Haines<sup>13</sup>, Scott T. Kay<sup>14</sup>, Lorenzo Lovisari<sup>10,15</sup>, Ben J. Maughan<sup>16</sup>, Etienne Pointecouteau<sup>17</sup>, Elena Rasia<sup>18,19,20</sup>, Mario Radovich<sup>21</sup>, and Jack Sayers<sup>22</sup>

<sup>1</sup> Dipartimento di Fisica G. Occhialini, Università degli Studi di Milano Bicocca, Piazza della Scienza 3, I-20126 Milano, Italy

<sup>2</sup> Instituto de Astrofísica de Canarias, C/ Vía Láctea s/n, E-38205 La Laguna, Tenerife, Spain

<sup>3</sup> Universidad de La Laguna, Departamento de Astrofísica, E-38206 La Laguna, Tenerife, Spain

<sup>4</sup> INAF – Osservatorio di Astrofisica e Scienza dello Spazio di Bologna, via Piero Gobetti 93/3, I-40129 Bologna, Italy

<sup>5</sup> INFN, Sezione di Bologna, viale Berti Pichat 6/2, I-40127 Bologna, Italy

<sup>6</sup> Dipartimento di Fisica ‘E. Pancini’, Università degli Studi di Napoli Federico II, Via Cinthia, 21, I-80126 Napoli, Italy

<sup>7</sup> Université Côte d’Azur, Observatoire de la Côte d’Azur, CNRS, Laboratoire Lagrange, Bd de l’Observatoire, CS 34229, 06304 Nice Cedex 4, France

<sup>8</sup> Université Paris-Saclay, Université Paris Cité, CEA, CNRS, AIM, 91191 Gif-sur-Yvette, France

<sup>9</sup> Michigan State University, Physics and Astronomy Department, 567 Wilson Road, East Lansing, Michigan 48824, USA

<sup>10</sup> INAF, Istituto di Astrofisica Spaziale e Fisica Cosmica di Milano, via A. Corti 12, 20133 Milano, Italy

<sup>11</sup> Laboratoire d’Astrophysique de Marseille, Aix-Marseille Univ., CNRS, CNES, 13013 Marseille, France

<sup>12</sup> Institut d’Astrophysique de Paris, UMR7095 CNRS & Sorbonne Université, 98bis Bd Arago, 75014, Paris, France

<sup>13</sup> Instituto de Astronomía y Ciencias Planetarias, Universidad de Atacama, Copayapu 485, Copiapó, Chile

<sup>14</sup> Jodrell Bank Centre for Astrophysics, Department of Physics and Astronomy, University of Manchester, Manchester M13 9PL, UK

<sup>15</sup> Center for Astrophysics | Harvard & Smithsonian, 60 Garden Street, Cambridge, MA 02138, USA

<sup>16</sup> HH Wills Physics Laboratory, University of Bristol, Tyndall Ave, Bristol, BS8 1TL, UK

<sup>17</sup> IRAP, CNRS, Université de Toulouse, CNES, Toulouse, France

<sup>18</sup> Osservatorio Astronomico di Trieste, via Tiepolo 11, I-34131, Trieste, Italy

<sup>19</sup> IFPU, Institute for Fundamental Physics of the Universe, Via Beirut 2, 34014 Trieste, Italy

<sup>20</sup> Department of Physics; University of Michigan, Ann Arbor, MI 48109, USA

<sup>21</sup> INAF - Osservatorio Astronomico di Padova, vicolo Osservatorio 5, I-35122, Padova, Italy

<sup>22</sup> California Institute of Technology, Pasadena, CA 91125 USA

Received XXX; accepted XXX

## ABSTRACT

We analyse the kinematical properties of the CHEX-MATE (Cluster HERitage project with XMM-Newton – Mass Assembly and Thermodynamics at the Endpoint of structure formation) galaxy cluster sample. Our study is based on the radial velocities retrieved from SDSS-DR18, DESI and NED spectroscopic databases and new data obtained with the 10.4m GTC or the ESO-NTT telescopes. We derive cluster mass profiles for 75 clusters using the MG-MAMPOSSt procedure, which recovers the gravitational potential and the anisotropy profiles from line-of-sight velocities and projected positions of galaxy members. The standard NFW and the Burkert models with flatter cores than NFW both adequately fit the kinematic data, with only marginal statistical preference for one model over the other. An estimation of the mass bias  $(1 - B_1) = M_{500}^{SZ}/M_{500}^M$  is performed from the comparison with SZ-X-ray-calibrated mass estimates, resulting in a value of  $0.54 \pm 0.11$  when four evidently disturbed clusters are removed from the sample. We assess the dynamical state of the clusters by inferring the Anderson-Darling coefficient ( $A^2$ ) and the fraction of galaxies in substructures ( $f_{\text{sub}}$ ). Except for a few cases, we found relatively low values for  $A^2$ , suggesting that CHEX-MATE clusters are not too far from relaxation. Moreover, no significant trends emerge among  $A^2$ ,  $f_{\text{sub}}$  and the difference between the log-masses estimated by MG-MAMPOSSt and by SZ-X-ray. We study the concentration-mass relation for the sample; despite the large scatter, we observe signs of an increasing trend for large-mass clusters, in agreement with recent theoretical expectations. Finally, the analysis of radial anisotropy profiles of member galaxies - stacked in five bins of mass and redshift - reveals that orbits tend to be isotropic at the center and more radial towards the edge, as already found in previous studies. A slight trend of increasing radial orbits at  $r_{200}$  is observed in clusters with larger velocity dispersion.

**Key words.** galaxies: clusters: general — galaxies: kinematics and dynamics

## 1. Introduction

Galaxy clusters are the most massive virialised structures in the Universe, so they are excellent natural laboratories to study

<sup>★</sup> Based in part on observations collected at the European Southern Observatory under ESO programmes 0110.A-4192 and 0111.1-0186.

the formation, structure assembly, and evolution of mass halos and subhalos across the cosmic time. The combination of optical data, X-ray observations, and the signal from Sunyaev-Zel'dovich (SZ) Effect (Sunyaev & Zeldovich 1972) provides the ideal scenario to study galaxy clusters. A multi-wavelength analysis will allow us to acquire a complete panorama from the physics behind different components: Dark Matter (DM; Zwicky 1933), gas (Cavaliere & Fusco-Femiano 1981), and galaxies (e.g., Abell 1958), and see how they interact to configure these such massive objects.

In this work we study dynamical cluster mass profiles, the presence of substructures, and velocity anisotropies by analysing the projected phase-space distribution of member galaxies (e.g., Carlberg et al. 1997) under the assumption of dynamical equilibrium. In fact, as galaxies enter into clusters through hierarchical accretion, their orbits contain important information on the processes that lead to the cluster mass assembly and internal dynamical relaxation (e.g., Biviano & Katgert 2004). Moreover, knowledge of the orbits of cluster galaxies is crucial to understand environmental effects that differentiate galaxy evolution in clusters relative to the field (Lotz et al. 2019; Tonnesen 2019).

Our studies are carried out using the MG-MAMPOSST (Modelling Anisotropy and Mass Profile of Spherical Observed Systems) code of Pizzuti et al. (2023). This technique allows us to obtain a cluster mass profile reconstruction and the velocity anisotropy profile for several parametrisations of the total gravitational potential, in GR and in general dark energy or modified gravity frameworks. In other words, MG-MAMPOSST jointly obtains the best fit parameters for the cluster mass distribution and for the velocity anisotropy profile of cluster members (Munari et al. 2014; Zarattini et al. 2021); this analysis allows us to retrieve information about orbits of galaxies, by distinguishing, statistically, between populations with radial and/or circular configurations.

We developed our analysis in the CHEX-MATE cluster sample (CHEX-MATE Collaboration et al. 2021), the Cluster Heritage project with XMM-Newton – Mass Assembly and Thermodynamics at the Endpoint of structure formation. This project is based on the three-mega-second Multi-Year Heritage Programme to obtain X-ray observations of a minimally-biased, signal-to-noise-limited (SNR > 6.5) sample of 118 galaxy clusters detected by *Planck* through the SZ effect. The CHEX-MATE census contains two subsamples: the Tier 1, which includes a census of the population at the most recent time ( $0.05 < z < 0.2$ ); and the Tier 2, the most massive objects to have formed at  $z < 0.6$  (see Fig. 1 in CHEX-MATE Collaboration et al. 2021). Hereafter, we will refer to Tier 1 and Tier2 as T1 and T2, respectively. Therefore, the CHEX-MATE clusters offers us the opportunity to study the kinematical and dynamical properties of the most massive clusters of the Universe detected through their SZ signal.

The masses of galaxy clusters can be obtained directly under specific assumptions (see e.g. Pratt et al. 2019). Usually, X-ray mass estimates can be recovered either by assuming the hydrostatic equilibrium (see e.g. Ettori et al. 2013) or through scaling relations among integrated quantities, like gas mass and temperature (e.g. Kravtsov et al. 2006). The SZ effect can also be used to estimate masses through the Comptonization parameter,  $Y_{SZ}$ .

Here, we adopt a dynamical method that uses the line-of-sight velocities of member galaxies and their projected positions with respect to the cluster center to directly measure the mass. Different mass estimation techniques could be biased due to various effects, such as violation of the assumption of hydrostatical or dynamical equilibrium, or asymmetric, complicated true geometries. To account for these deviations for all these methods,

we will study the mass bias parameter  $(1 - B_1) = M_{500}^{SZ}/M_{500}^M$  (Ruel et al. 2014; Penna-Lima et al. 2017; Amodeo et al. 2017), in order to characterise the cluster mass estimations when these are performed using the SZ-X-ray signature or other dynamical techniques. In particular, we will refer to the SZ-X-ray-calibrated mass estimates as  $M^{SZ}$ , while the mass derived by the MG-MAMPOSST analysis are identified by  $M^M$ .

Our main aims can be summarized in three points: 1) obtain the full kinematic mass profiles for the CHEX-MATE clusters, which allows future comparisons with those obtained from X-ray, SZ and weak-lensing techniques; 2) study the scaling relations and presence of possible biases in the mass estimates derived from different techniques; 3) study statistically the main kinematical properties of the cluster members, by disentangling their velocity anisotropy and orbits depending of the mass of the clusters.

Throughout this paper, we adopt a  $\Lambda$ CDM cosmology with  $\Omega_m = 0.3$ ,  $\Omega_\Lambda = 0.7$ , and  $H_0 = 70 \text{ km s}^{-1} \text{ Mpc}^{-1}$ . We further define  $r_\Delta \equiv r_{\Delta c}$  as the radius of a spherical overdensity within which the mean density is  $\Delta$  times the critical density of the universe. The corresponding enclosed mass is  $M_\Delta$  (e.g.,  $r_{200}$ ,  $M_{200}$  for  $\Delta = 200$ , and so on). Logarithms in base 10 are defined as:  $\text{Log } X = \log_{10} X$ , for any variable  $X$ , while natural logarithms are indicated by  $\ln X$ .

## 2. Dataset

Our analysis is based on the radial velocities of cluster members. However, not all the 118 clusters of the CHEX-MATE sample have spectroscopic data of sufficient quality to enable the analysis. So, we restrict our study to 75 clusters, which correspond to a subset of galaxy systems providing at least 50 confirmed members within an aperture radius  $R = r_{\text{ap},200}$  - as estimated by Sereno et al. (2025) - with spectroscopic redshifts, which is a reasonable minimum number of members to obtain an accurate enough analysis of the mass and dynamical properties (see e.g., Ferragamo et al. 2020). As stated in Sereno et al. (2025), the cluster centre has been identified as the X-ray luminosity peak. As shown in Fig. 1, this subsample represents the 66% of the full CHEX-MATE clusters, with no bias in redshift or mass. In this Figure the sample is divided into redshift bins (with width equal to 0.05) and mass bins (with width equal to  $10^{14} M_\odot$ ), our analysis covers more than 50% of the CHEX-MATE clusters in each bin, with the exception of those with  $z > 0.55$ . In other words, the full CHEX-MATE sample is well represented in the present work. Most of the clusters present a large number of members with spectroscopic redshifts, with more than 100 confirmed members within 4.0 Mpc in the majority of the cases, and even more than 300 for some of them. PSZ2 G006.49+50.56 (Abell 2029) and PSZ2 G044.20+48.66 (Abell 2142) represent outstanding cases with more than 1000 total spectroscopic redshifts available.

The cluster member selection for the sample used in this work was developed by Sereno et al. (2025) using the CLEAN method (fully described in Mamon et al. 2013, see Appendix B), which is based on galaxy location in the projected phase-space. So, the radial velocities of cluster members are the same as used in Sereno et al. (2025), who base their analysis on the SDSS-DR18, DESI, and NED databases, in addition to some private catalogues and proprietary data. Moreover, we add new spectroscopic observations<sup>1</sup> for three CHEX-MATE clusters. These are

<sup>1</sup> These new dataset will be made publicly available soon, but it is already available upon request. An extract can be found in Appendix D.

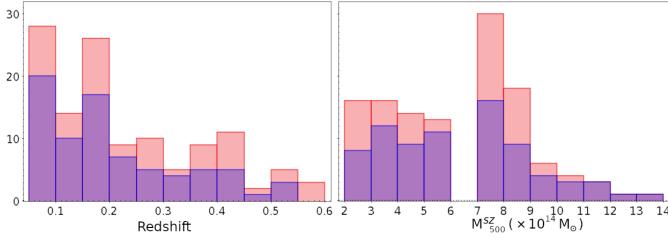


**Fig. 1.** Cluster redshift and  $M_{500}^{SZ}$  mass distributions of the full CHEX-MATE sample (red) and the considered subsample (blue).  $M_{500}^{SZ}$  has been derived iteratively from the  $Y_{SZ} - M_{500}^{SZ}$  relation calibrated using hydrostatic masses obtained from XMM-Newton data (see CHEX-MATE Collaboration et al. 2021).

PSZ2 G113.91-37.01, PSZ2G046.10+27.18, and PSZ2G083.29-31.03, all of them in the redshift range  $0.37 < z < 0.41$ . We observed galaxies in these fields at the 10.4m GTC telescope with the OSIRIS spectrograph in multi-object observing mode acquiring 2400 s exposures and two mask configurations for each cluster. For more details on the instrumental set-up, data reduction process, and redshift estimates, see Ferragamo et al. (2020) and Aguado-Barahona et al. (2022). The procedures applied in this work are exactly the same as those used there. So, we obtain radial velocities for 80, 61 and 66 cluster members, respectively, with a precision of about  $70 \text{ km s}^{-1}$ . These spectroscopic observations are quite limited, showing magnitude limits of  $r' \sim 21.5$ , and low sample completeness, below 30% within  $r_{500}$ .

For these three clusters we select members by applying a  $2.7\text{-}\sigma$  clipping in the phase-space, to minimise the fraction of interlopers<sup>2</sup> (Mamon et al. 2010). However, we found that only PSZ2G046.10+27.18 has more than  $N = 50$  members within the estimated  $r_{200}$ . From now on, we refer to  $r_{200,ap}$  as the radius provided by the CLEAN procedure, to distinguish it from the values obtained by the MG-MAMPOSS<sub>T</sub> fit.

In summary, including the GTC observations, we manage 77 catalogs of cluster member galaxies (one for each cluster), with a total of 17521 radial velocities, which yields a mean of about 220 members per cluster. Among these, 75 clusters have found to provide  $N \geq 50$  confirmed members within the aperture radius  $R = r_{200,ap}$ , after the application of the CLEAN algorithm (Sereno et al. 2025). Considering this spectroscopic dataset, we present in the following sections our procedure to analyse the main kinematical and dynamical properties of the CHEX-MATE cluster sample.

### 3. Kinematics analysis setup

We infer the cluster mass profiles of the CHEX-MATE sample by employing the MG-MAMPOSS<sub>T</sub> (Modelling Anisotropy and Mass Profile of Spherical Observed Systems) method (Pizzuti et al. 2023), which is based on the MAMPOSS<sub>T</sub> (Mamon et al. 2013) algorithm to simultaneously recover the (total) gravitational potential and the orbit anisotropy profile of clusters from kinematic analyses of their member galaxies.

MAMPOSS<sub>T</sub> is based on the assumption that the system is spherically symmetric and that galaxies are collisionless tracers of the gravitational potential. In this case, the dynamics is determined by the so-called (spherical) Jeans' equation:

$$\frac{d(v\sigma_r^2)}{dr} + 2\beta(r)\frac{v\sigma_r^2}{r} = -v(r)\frac{d\Phi}{dr}, \quad (1)$$

where  $r$  indicates the 3D radial distance from the cluster center,  $v(r)$  is the number density profile of galaxies,  $\sigma_r^2$  is the velocity dispersion along the radial direction, and  $\Phi$  is the total gravitational potential. The quantity  $\beta \equiv 1 - (\sigma_\theta^2 + \sigma_\phi^2)/2\sigma_r^2$  is the velocity anisotropy, with  $\sigma_\theta^2$ ,  $\sigma_\phi^2$  the velocity dispersion components along the tangential and azimuthal directions, respectively. In spherical symmetry, we have  $\sigma_\theta^2 = \sigma_\phi^2$ .

MAMPOSS<sub>T</sub> and MG-MAMPOSS<sub>T</sub> work in the so-called projected phase-space ( $R, v_{los}$ ), PPS hereafter, with  $R$  the projected radial distance from the cluster centre - defined to be at the peak of the projected X-ray emission (Sereno et al. 2025) - and  $v_{los}$  the line-of-sight (LOS) velocity of each galaxy, computed in the rest frame of the cluster. Given as input the parametric expressions of the gravitational potential, the number density profile, and the velocity anisotropy profile, the code implements a maximum likelihood fit to determine the best set of parameters describing the PPS distribution of cluster members.

MG-MAMPOSS<sub>T</sub> extends the gravitational potential models available in the original MAMPOSS<sub>T</sub>, further including generalized models of the velocity anisotropy profile, which we explore here. MG-MAMPOSS<sub>T</sub> also includes popular modified gravity and alternative Dark Energy scenarios (see Pizzuti et al. 2021 for a description of the physics), viable at the cosmological level, which we do not analyse in this paper. Moreover, a recent update of the code implemented a module to include data of the velocity dispersion of the brightest cluster galaxy (BCG) in the fit, when available. Inclusion of the BCG velocity dispersion would allow the method to provide tight constraints on the slope of the dark matter profiles in clusters (see Biviano et al. 2023). However, in this work, we will not use the BCG module.

Therefore, we only consider galaxies outside of a minimum projected radius  $R_{min} = 0.05 \text{ Mpc}$ . The central region is excluded to avoid contamination by the BCG which dominates cluster dynamics at very small radii. Furthermore, in its current implementation, MG-MAMPOSS<sub>T</sub> assumes negligible streaming motions and a Gaussian 3D velocity distribution of the tracers.

We run MG-MAMPOSS<sub>T</sub> over our CHEX-MATE subsample of 75 clusters including members up to a maximum projected radius  $R_{max} = 1.1 r_{200}^D$ , where  $r_{200}^D$  is the estimate of the (dynamical) virial radius coming either from the analysis of Sereno et al. (2025) ( $r_{ap,200}$ ) or directly from the velocity dispersion (see Sect. 5 in Barrena et al. 2024) for those clusters for which the former is not available. This definition of maximum radius for cluster membership is a common choice to ensure the validity of the Jeans equation, as  $r_{200}$  is close to the virial radius within Eq. (1) holds.

We sample the parameter space with a MCMC Metropolis-Hastings algorithm for 110 000 points, considering the first 10 000 as the burn-in phase. Our final chain contains 100 000 samples for each run; this number has been chosen has a reasonable value to save computational time while ensuring convergence. In more detail, we checked convergence by considering the four clusters with the fewest members ( $N < 60$ ) within  $r_{ap,200}$ ; and running  $n = 5$  test chains for each of them. We then computed the corresponding Gelman-Rubin diagnostic coefficients  $\hat{R}$  Gelman & Rubin (1992)<sup>3</sup> checking that the requirement  $\hat{R} \leq 1.1$  is always satisfied, as done in Pizzuti et al. (2024).

<sup>2</sup> Galaxies not belonging to the clusters falling inside the projected phase-space.

<sup>3</sup> the Gelman-Rubin coefficient is defined as  $\hat{R} = [W(L-1)/L + B/L]/W$ , where  $L$  is the length of the chains,  $B$  the variance of the

As for the main analysis, a total of eight MG-MAMPOSST chains are generated per cluster in the sample, exploring the combination of two models for the number density distribution and four models for the total mass profile, which we list in the following. The Navarro-Frenk-White (NFW) model can be written as,

$$M_{\text{NFW}}(r) = M_{200} \frac{\ln(1 + r/r_s) - r/r_s/(1 + r/r_s)}{\ln(1 + c_{200}) - c_{200}/(1 + c_{200})}, \quad (2)$$

where  $M_{200} = 200 (H^2(z)/2G) r_{200}^3$  is the enclosed mass at  $r_{200}$  and  $c_{200} = r_{200}/r_{-2}$  is the concentration, with  $r_{-2}$  being the radius at which the logarithmic slope of the density profile is  $-2$ . For the NFW model, this radius corresponds to  $r_s$ .

The Hernquist profile has a steeper decline of the density at large radii, and the mass enclosed in a radius  $r$  reads (Hernquist 1990),

$$M_{\text{Her}}(r) = M_{200} \frac{r_s^2 + r_{200}^2}{r_{200}^2} \frac{r^2}{r + r_{200}^2}, \quad (3)$$

where  $r_s = 2 r_{-2}$ .

The Burkert model (Burkert 1995) has a central core in the density distribution, and the mass is given by

$$M_{\text{Bur}}(r) = \frac{M_{200} \left[ \ln((r/r_s)^2 + 1) + 2 \ln(r/r_s + 1) - 2 \tan^{-1}(r/r_s) \right]}{\left[ \ln((r_{200}/r_s)^2 + 1) + 2 \ln(r_{200}/r_s + 1) - 2 \tan^{-1}(r_{200}/r_s) \right]}, \quad (4)$$

with  $r_s \simeq r_{-2}/1.5$ .

Finally, the Einasto model Einasto (1965) can be written as,

$$M_{\text{Eis}}(r) = M_{200} \frac{\gamma \left[ \frac{3}{m}, \frac{2}{m} \left( \frac{r}{r_s} \right)^m \right]}{\gamma \left[ \frac{3}{m}, \frac{2}{m} (c_{200})^m \right]}, \quad (5)$$

where we set the shape parameter<sup>4</sup>  $m = 3$  and  $r_s = r_{-2}$  as for the NFW profile. Therefore, all models are described by two free parameters, the mass  $M_{200}$  (or equivalently, the radius  $r_{200}$ ) and the scale radius  $r_s$ , which will be fitted within the MG-MAMPOSST algorithm.

As mentioned above, we further consider two models for the number density profile: the projected NFW and the projected Hernquist (pNFW and pHer, respectively). These models are defined as the integral of Eqs. (2),(3) along the LOS. While the profiles are characterized by two free parameters, only the scale radius  $r_v$ <sup>5</sup> is relevant in the analysis, as the other factors out in the solution of the Jeans equation implemented in MG-MAMPOSST. Note that for  $r_v$ , we first perform a preliminary fit to the member galaxy distribution in the phase space which does not require the binning of data (Sarazin 1980), assuming a constant completeness of the sample in the projected radial distance explored. This last assumption is rather strong, since our dataset exhibits quite incomplete and inhomogeneous spatial distributions; however, we carried out a detailed analysis on a few clusters to check that reasonable variation of the completeness does not provide relevant changes in the reconstructed mass profile.

means of the chains, and  $\overline{W}$  the averaged variances of the individual chains across all chains.

<sup>4</sup> We checked that varying the exponent between  $m = 2$  and  $m = 5$  does not lead to statistically relevant changes in the final posterior.

<sup>5</sup> we define the scale radius of the number density profile as  $r_v$  to avoid confusion with that of the mass profile

We then use the 95% C.L. limits of the inferred  $r_v$  as the upper and lower bounds for the flat prior range in the MG-MAMPOSST fit (see below). We have further checked that varying this interval produces negligible effects in the reconstructed mass profile.

As for the velocity anisotropy profile, we adopt a generalized Tiet (gT hereafter, see Mamon et al. 2019) model, which is an extension of the Tiet profile (Tiet et al. 2007) able to capture a quite broad ranges of possibilities for the orbits of member galaxies in clusters:

$$\beta_{gT}(r) = \beta_0 + \beta_\infty r/(r + r_\beta), \quad (6)$$

where  $\beta_0$  and  $\beta_\infty$  are the inner and outer values of the anisotropy, respectively, and  $r_\beta$  is a characteristic scale radius. In all cases, we set  $r_\beta = r_{-2}$  (i.e., the scale radius of the mass profile) as suggested by numerical simulations (Mamon et al. 2010). In MG-MAMPOSST, we work with the rescaled parameters  $\mathcal{A}_{0,\infty} = (1 - \beta_{0,\infty})^{-1/2}$ , which are equal to one for completely isotropic orbits.

We adopt flat priors on all the fitted parameters,  $r_{200}/\text{Mpc} \in [0.5, 5.0]$ ,  $r_s/\text{Mpc} \in [0.04, 4.0]$ ,  $\mathcal{A}_{0,\infty} \in [0.4, 7.0]$ ,  $r_v \in [r_v^{\text{low}}, r_v^{\text{up}}]$ , where the last range is between the 95% lower and upper limits from the external fit of the projected number density distribution. Except for  $r_v$ , the priors are non-informative.

For each posterior, we apply the Bayesian Information Criterion (BIC hereafter, see, e.g., Mamon et al. 2019) to quickly select the best model among the eight combinations analysed:

$$\text{BIC} = k \ln N - 2 \ln \mathcal{L}, \quad (7)$$

where  $k$  is the number of free parameters,  $N$  the number of data-points and  $\mathcal{L}$  the likelihood at the best fit. Generally, a model is said to be strongly preferred when its BIC is lower by a factor of  $\sim 6$  with respect to the others. For the models with the same number of free parameters, the BIC comparison is equivalent to the chi-square  $\chi^2$  comparison. It is important to stress that MG-MAMPOSST only indicates which model is favored relative to the others, but not the best model in an absolute sense. We further quantify the systematics induced by the modeling as half of the maximum variation between all the best-fit values of each parameter.

## 4. Results

Here we present the main outcomes from the MG-MAMPOSST analysis for the CHEX-MATE sample of 75 clusters. Among the mass ansatz, all the models adequately fit the PPS distribution, with the NFW profile performing better for 45% of the clusters, followed by Burkert (32.5%), Einasto (12.5%), and Hernquist (8%). This distribution may indicate a slight preference towards steeper central profiles with respect to those with cores. While it is true that the presence of interlopers that survived the CLEAN procedure can produce a steeper profile, thus biasing in favor of NFW-like models, the statistical significance of the latter is in general negligible, with very small  $\Delta\text{BIC}$  ( $\lesssim 1.0$  on average). In contrast, the fits to the number density distribution of galaxies notably prefer the projected Hernquist model compared to the NFW model for more than 70% of the analysed clusters, with several cases where  $\Delta\text{BIC} \gtrsim 6.0$ . This preference seems to be in contrast to other studies (e.g. van der Burg et al. 2016), which indicate a preference of the pNFW model. However, one should note here that the assumption of a constant completeness may play a significant role. Indeed, while it is true that the constraints on a mass profile distribution are not strongly affected by the

choice of the model of the number density profile in the MG-MAMPOSST fit, the slope of  $\nu(r)$  and the value of the scale radius  $r_\nu$  depends on the completeness. In order to deal with this issue, one should compute the completeness, cluster by cluster, by comparing photometric and spectroscopic catalogs. However, this analysis is beyond the scope of the paper. As an example, we consider the case of the cluster PSZ2 G049.22+30.8, for which the completeness as a function of the projected radius has been estimated according to the model

$$C(R) = A \exp(BR), \quad (8)$$

with  $A = 0.817$ ,  $B = -0.413$ . While in this case the best fit projected number density is always a NFW profile, the value of the scale radius changes from  $r_\nu = 0.31^{+0.18}_{-0.10}$  when accounting for the correct completeness, to  $r_\nu = 0.59^{+0.10}_{-0.13}$ , when a constant completeness is assumed (uncertainties are given at 95% C.L.).

In Table A.1 we report the regression results. In the second and third columns, we list the best fit models (i.e., the models that give the highest posterior) for mass and density, respectively. For each entry, the first uncertainties refer to the (statistical) 95% confidence intervals, while the second values are the systematic uncertainties computed as discussed above. The last four columns show the value of the log posterior  $\ln P$  of the best fit, the cluster redshift  $z$ , the value of the Anderson-Darling coefficient  $A^2$  (see Sect. 4.3), and the estimated line-of-sight velocity dispersion at  $r_{200}$ ,  $\sigma_{\text{ap},200}$ . Note that the MG-MAMPOSST procedure is pretty robust in estimating  $r_{200}$  against the choice of the mass, anisotropy and number density models, as shown by the small systematic uncertainties compared with the statistical errors.

In Fig. 2 we show an example of the mass and anisotropy profiles obtained from MG-MAMPOSST for one rich cluster ( $N_{\text{gal}} = 291$  spectroscopic members within  $r_{\text{ap},200}$ ) in the sample, PSZ2 G067.17+67.46. The mass is parametrized as an NFW model, which gives the best-fit profile, with a pNFW model for the number density of the member galaxies.

We then compute the mass inside the virial radius as  $M_{200} = (100 H^2(z)/G) \times r_{200}^3$ , and we perform a first comparison with the results of Sereno et al. (2025). Fig. 3 displays the values of  $\text{Log } M_{200}$  as obtained by MG-MAMPOSST (vertical axis), and  $\text{Log } M_{\sigma,200c}$  estimated from the aperture velocity dispersion  $\sigma_{\text{ap},200}$  with the method of Sereno et al. (2025) (horizontal axis). The superscript ( $M$ ) refers to the MG-MAMPOSST estimates.

The results show an overall good agreement among the two estimates, confirming the robustness of the simpler analytical approach of Sereno et al. (2025). However, for seven clusters MG-MAMPOSST tends to overestimate  $M_{200}$  with respect to the findings of Sereno et al. (2025). For those clusters we found an average logarithmic difference  $\text{Log } M_{200}^M - \text{Log } M_{\sigma,200c} > 0.3$  dex.

If we look at the relation between  $M_{200}^M$  and the aperture velocity dispersion  $\sigma_{\text{ap},200}$  (Fig. 4) obtained by Sereno et al. (2025) using the CLEAN method (Mamon et al. 2013), it is easy to see that six of the seven clusters are characterized by large values of  $\sigma_{\text{ap},200} > 10^3$  km/s. This pattern suggests that clusters in the CHEX-MATE sample with very large velocity dispersion may suffer a stronger contamination of interlopers. This fact was first found by Mamon et al. (2010) who, working with simulated halos, found that the fraction of interlopers should be (slightly) more important in the more massive halos since they have (slightly) lower concentrations (Navarro et al. 1997; Maciò et al. 2008) and they typically live in richer environments. That is, the larger fraction of interlopers that survived the membership selection performed by Sereno et al. (2025) in high-mass

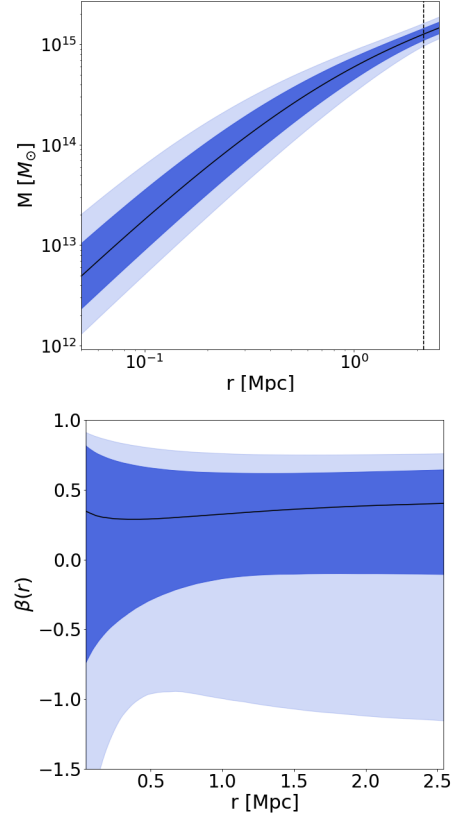


**Fig. 2.** Mass profile (top) and radial velocity anisotropy profile (bottom) of the cluster PSZ2 G067.17+67.46, as obtained by the MG-MAMPOSST analysis with  $N_{\text{gal}} = 299$  galaxies adopting a NFW and a gT models, respectively. In both plots, darker and lighter shaded regions refer to 68% and 95% confidence levels, respectively. The vertical dashed line in the top panel identifies the best fit for  $r_{200} = 2.19$  Mpc.

clusters could translate into a higher mass estimation by MG-MAMPOSST - which is a more complex model with respect to that of Sereno et al. (2025) - for the most massive systems.

Moreover, in MG-MAMPOSST the concentration  $c_{200} = r_{200}/r_{-2}$  is a free parameter (or better, it is a quantity derived from two parameters optimized within the fit), while in Sereno et al. (2025) it is fixed as a function of  $r_{200}$  using the concentration-mass relation proposed by Diemer & Joyce (2019).

As shown by the blue points in Fig. 8, the off-trend clusters are characterized by a concentration estimated by MG-MAMPOSST that is lower than the prediction of Diemer & Joyce (2019) (brown solid line), consequently boosting the reconstructed  $M_{200}$ .

The blue line in Fig. 4 shows the best orthogonal distance regression (ODR) fit for the linear model

$$\text{Log} \left( F_z \frac{M_{200}^M}{10^{14} M_\odot} \right) = \alpha_\sigma \text{Log} \left( \frac{\sigma_{\text{ap},200}}{10^3 \text{ km s}^{-1}} \right) + \beta_\sigma + \gamma_\sigma \text{Log } F_z, \quad (9)$$

when fixing the redshift to the pivot value of the sample  $z_p = 0.2$ ; in eq. (9),  $F_z = H(z)/H(z_p)$ . We found:

$$\alpha_\sigma = 3.61 \pm 0.17, \quad \beta_\sigma = 1.07 \pm 0.01, \quad \gamma_\sigma = -0.83 \pm 0.70, \quad (10)$$

which is slightly steeper than  $\alpha \sim 3$ , as in e.g., Munari et al. (2013); Ferragamo et al. (2020). If we consider the T1 and T2 clusters separately, the ODR fit of Eq. (9) provides a slightly



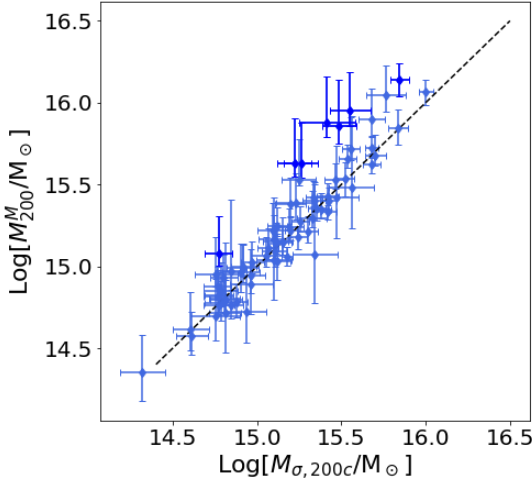


**Fig. 3.** Scatter plot of  $\text{Log } M_{200}$ , inferred from the kinematic analysis with MG-MAMPOSS $\tau$  (vertical axis), and  $\text{Log } M_{\sigma, 200c}$  obtained by Sereno et al. (2025) (horizontal axis). The errorbars represent the 68% C.L., while the black dashed line indicates the bisector. Darker points highlight those clusters for which  $\text{Log}(M_{200}^M / M_{\sigma, 200c}) > 0.3$ .

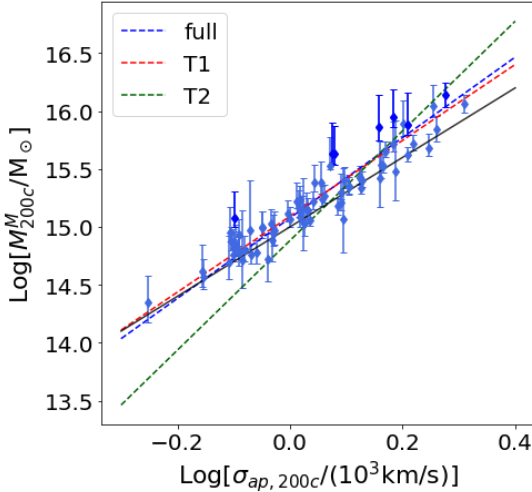


**Fig. 4.** Logarithm of the aperture velocity dispersion within  $R = r_{200}$ ,  $\sigma_{ap, 200}$  compared to the logarithm of  $M_{200}^M$  estimated from MG-MAMPOSS $\tau$ . The bars refer to 68% uncertainties. The blue line indicates the best fit linear model of eq. (9) when  $z = 0.2$ . The black solid line identifies the  $\sigma \propto M^3$  relation.

lower  $\alpha^{T1} = 3.31 \pm 0.17$  for the Tier 1 sample - close to the  $\sim \sigma^3$  relation and a higher value  $\alpha^{T2} = 4.81 \pm 0.64$  for Tier 2. This reflects the fact that T2 contains massive clusters by construction, and that among the seven off-trend objects, five belong to T2. The best ODR fits for  $z_p$  are shown as the red and green dashed lines for T1 and T2 respectively.

#### 4.1. Comparison with SZ mass estimates

In order to compare our kinematic masses with the ones obtained from the SZ effect, we further derive the distribution of  $M_{500} = 500 H^2(z)/(2G) \times r_{500}^3$ , as follows: for each value of  $r_{200}$ ,  $r_s$  in the MCMC chain we obtain the corresponding parametric mass profile  $M(r|r_{200}, r_s)$ . The radius  $r_{500}$  is then given by

the numerical solution of the equation

$$\frac{M(x)}{x^3} = \frac{500 H^2(z)}{2G}. \quad (11)$$

From that, the computation of  $M_{500}$  is straightforward.

In Figure 5 we plot the values of  $\text{Log } M_{500}$  as obtained by MG-MAMPOSS $\tau$  (vertical axis) and inferred by SZ (horizontal axis), where the superscript ( $M$ ) and ( $SZ$ ) refers to the MG-MAMPOSS $\tau$  and SZ estimates respectively. We found a quite strong correlation between the two estimates (Pearson coefficient  $r = 0.68$ , p-value  $< 10^{-5}$ ); we fit the linear relation

$$\text{Log} \left( \frac{M_{500}^{SZ}}{10^{14} M_\odot} \right) = \alpha_{SZ} \text{Log} \left( \frac{M_{500}^M}{10^{14} M_\odot} \right) + \text{Log}(1 - B), \quad (12)$$

where the mass-dependent bias  $(1-B)$  is defined similarly to that done, for example, in Ferragamo et al. (2021) and Aguado-Barahona et al. (2022). This way, the usual bias  $(1 - B_1) = M_{500}^{SZ}/M_{500}^M$  is recovered when  $\alpha_{SZ} = 1$ .

We obtain  $\alpha_{SZ} = 0.84 \pm 0.05$ , while an overall mass-dependent bias  $\text{Log}(1 - B) = -0.18 \pm 0.06$  dex is found when all the galaxy clusters in the sample are considered, corresponding to  $(1 - B) = 0.67 \pm 0.09$ ; this means that the kinematic results from MG-MAMPOSS $\tau$  produce larger masses with respect to those derived from the *Planck* SZ signal. This value seems to be in agreement within errors with those obtained by *Planck* Collaboration et al. (2020) and Lesci et al. (2023) from BAO and 3D clustering of the PSZ2 clusters. In addition, our estimate is similar to that found by the fit of Sereno et al. (2025), although slightly larger than that of Ferragamo et al. (2021) and Aguado-Barahona et al. (2022), who obtained a bias of  $(1 - B) \sim 0.80$  comparing *Planck* SZ-X-ray calibrated masses of 270 PSZ1 and 388 PSZ2 clusters, respectively, with the kinematic mass estimated through the total velocity dispersion. When forcing  $\alpha_{SZ}$  to unity, however, the difference among the two mass estimates is even larger, almost doubled:  $(1 - B_1) = 0.43 \pm 0.08$ , which is not consistent with the above mentioned works.

It is interesting to note that the sample includes a few clusters for which the kinematic mass is about one order of magnitude larger than the one given by the SZ proxy. We marked four clusters for which

$$\delta\eta = \text{Log } M_{500}^M - \text{Log } M_{500}^{SZ} > 0.8, \quad (13)$$

as red points in Figure 5. However, the PPS distributions of those clusters show evident sign of a disturbed dynamical state, as displayed in the left plots of Figure B.1, with very large velocity dispersions and presence of possible important structures that are not part of the main cluster, as in the case of PSZ2G056.77+36.32, and PSZ2G040.03+74.95.

The disturbed dynamical state of these four clusters is further indicated by the distributions of the velocities along the line of sight (central plots of Figure B.1), that for PSZ2G056.77+36.32 and PSZ2G040.03+74.95 exhibit a noticeable bimodal distributions. Note that, here we are considering the members selected by running the CLEAN algorithm in its default settings. However, as already done in Sereno et al. (2025), a refined analysis can be performed to study these systems. In more detail, PSZ2G040.03+74.95 - aka Abell 1831 - has been already identified as a double system: it is made of two clusters A,B at  $z = 0.063, 0.076$  respectively, nearly aligned along the line-of-sight, as discussed in Sereno et al. (2025). A similar situation holds for the object PSZ2G218.81+35.51 (see Sereno et al. (2025) and also the histogram of the LOS velocities in Figure

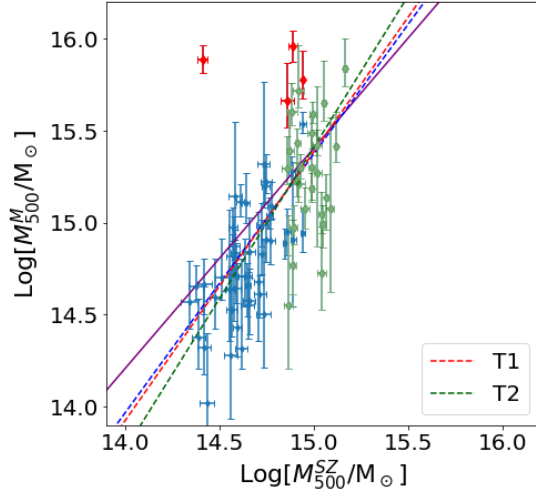


**Fig. 5.** Scatter plot of  $M_{500}$  inferred from SZ-effect by Planck (on the vertical axis) and from the kinematic analysis with MG-MAMPOSST (horizontal axis). The errorbars represent the 68% C.L. while the red points show those clusters for which the logarithmic difference ( $\delta\eta$ ) is larger than 0.8 dex. Dark-green points highlight clusters belonging to Tier 2. The purple line refer to a ODR fit considering all the clusters, while the blue one is the linear fit done by discarding the four above mentioned clusters. The best fits (with the four outliers removed) linear models for T1 and T2 separately are further shown as the red and dark-green dashed lines, respectively.

6). We found a logarithmic difference  $\delta\eta = 0.68 \pm 0.42$  for PSZ2G218.81+35.51, where the large uncertainties reflect the inefficiency of MG-MAMPOSST in fitting the double system with a single mass model.

By considering the two sub-groups in PSZ2G040.03+74.95 and PSZ2G218.81+35.51 as independent clusters<sup>6</sup>, the kinematical analysis gives  $M_{200} < 7 \times 10^{14} M_{\odot}$  and  $M_{200} = 53_{-26}^{+9} \times 10^{14} M_{\odot}$  for PSZ2G040.03+74.95 A, B, and  $M_{200} = 2.4_{-2.2}^{+1.8} M_{\odot}$ ,  $M_{200} = 6.1_{-2.7}^{+3.6} M_{\odot}$  for PSZ2G218.81+35.51 A, B. Note that for PSZ2G040.03+74.95 A we are able only to set an upper limit with MG-MAMPOSST, given the small number of members considered in the fit (only 25 members lie within  $R = r_{200}$ , well below the limit of 50 we imposed on the full sample) and the relatively small  $\sigma_{\text{ap},200} = 461 \text{ km s}^{-1}$ , compared to the error in the line-of-sight velocities. It is important to mention that the results for these bi-modal systems are in agreement (despite with larger uncertainties) with the values obtained by the simple halo model of Sereno et al. (2025).

For the most massive sub-components in the bimodal clusters (which are identified as the CHEX-MATE clusters, see Sereno et al. (2025) and references therein), the logarithmic difference is now reduced to  $\delta\eta = 0.8 \pm 0.3$  (PSZ2G040.03+74.95) and  $\delta\eta = 0.15 \pm 0.11$  (PSZ2G218.81+35.51), instead of 1.4 and 0.68. These interesting cases, as well the other three clusters mentioned above, deserve a separate detailed analysis of their properties. Such an analysis is beyond the scope of this paper and it will be performed in a separate work. From now on, we will consider only the main sub-components of the double systems in the forthcoming analyses.

If we remove the four clusters with large  $\delta\eta$  and we fit again eq. (12) (blue dashed line in Figure 5), we remarkably find a negligible mass-dependent bias within the uncertainties  $\text{Log}(1 - B) =$

<sup>6</sup> The selection of members for the subsystems is performed as discussed in Sereno et al. (2025)

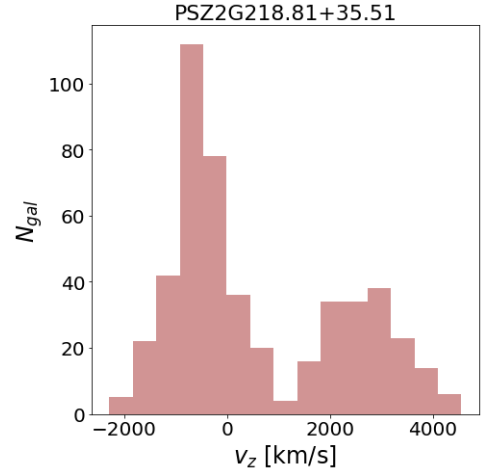


**Fig. 6.** LOS velocity distribution for the system PSZ2G218.81+35.51, made of two separate clusters, as mentioned in Sereno et al. (2025).

$0.02 \pm 0.04$ , which corresponds to  $1 - B = 1.04 \pm 0.09$ , with a slightly flatter slope  $\alpha_{\text{SZ}} = 0.71 \pm 0.04$ . Note that, however, the bias is still quite large when fixing the slope to 1,  $1 - B_1 = 0.54 \pm 0.11$ , from which we can conclude that kinematic mass estimates are a factor of two larger, on average, with respect to SZ probes. Note that this value is now in agreement with the findings of, e.g., Lesci et al. (2023). Here we have ignored the possible redshift dependence of the sample and neglected the Malmquist bias, both were already considered in Sereno et al. (2025). In particular, SZ masses are biased high, which may produce an underestimation of  $B$ . When considering separately T1 and T2 (after removing the four biased clusters) the fit is still consistent with a negligible mass-dependent bias; in particular,  $(1 - B) = 1.12 \pm 0.13$  for the former, while the latter provides  $(1 - B) = 1.32 \pm 0.44$ . The larger uncertainties in Tier 2 reflect a quite wide scatter in  $\delta\eta$ , as shown by the green points in Fig. 5. For  $B_1$ , we found  $(1 - B_1) = 0.64 \pm 0.04$  for Tier 1 and  $(1 - B_1) = 0.40 \pm 0.04$  for Tier 2.

Note that  $\delta\eta$  does not exhibit a strong correlation with redshift (see Fig. 7), with a quite scattered distribution. However, if we compute the fraction of galaxies with  $\delta\eta > 0.5$  in two redshift bins,  $z < 0.2$  and  $z > 0.2$ , we find 0.14 and 0.28, respectively. This difference should not come as a surprise, since clusters with  $z > 0.2$  belong to the Tier 2 selection, which contains massive clusters by construction (thus characterized by larger velocity dispersions, see, e.g., Sereno et al. (2025)). Those clusters exhibit overall larger discrepancies between  $M_{500}^{\text{SZ}}$  and  $M_{500}^{\text{M}}$ , attributed to a potentially stronger contribution of interlopers in the kinematics analysis, as already mentioned above, in clusters with high velocity dispersions.

#### 4.2. Concentration-mass relation

In Fig. 8 we plot the relation between  $c_{200}$  and  $M_{200}$  of the sample, as derived by the MG-MAMPOSST analysis. For the two double systems PSZ2G056.77+36.32 and PSZ2G218.81+35.51 we consider here separately the sub-components, further discarding PSZ2G056.77+36.32 A, given its limited statistics. Although the points appear quite scattered and have large uncertainties, a mild, positive correlation can be observed (Spearman rank coefficient 0.33, corresponding to a p-value of  $2 \times 10^{-3}$ ).

For a quantitative analysis, we perform a Bayesian regression. We follow the CoMaLit (Comparing Masses from Litera-

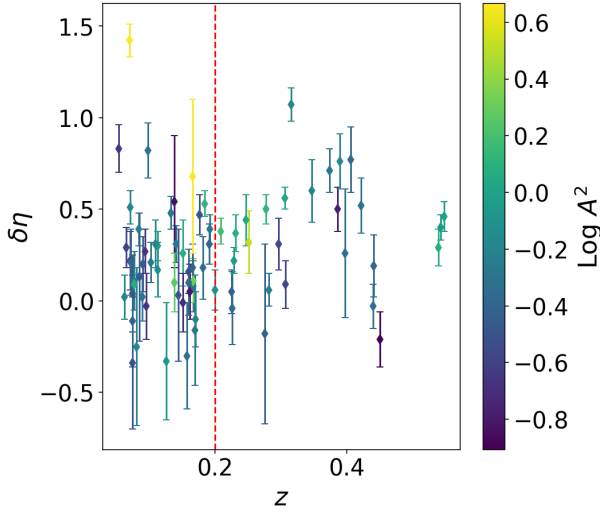


**Fig. 7.**  $\delta\eta \equiv \text{Log}(M_{500}^M/M_{500}^{SZ})$  as a function of the redshift. The error bars indicate the 68% statistical uncertainties. Points are color-coded according to the values of the  $A^2$  coefficient. The red vertical line indicates the pivot redshift  $z = 0.2$ .

ture) scheme described in Sereno & Ettori (2015b); Sereno et al. (2015a); Sereno & Ettori (2015a, 2017), which we refer to for details, and implemented in the R-package LIRA (Sereno 2016).<sup>7</sup>

The mass - concentration relation is modeled with a linear relation in log-space, similarly to eq. (9),

$$\text{Log}(c_{200}) = \alpha_C + \beta_C \text{Log}(M_{200}^M/M_{\text{pivot}}) + \gamma_C \text{Log} F_z, \quad (14)$$

where  $F_z = H(z)/H(z_{\text{ref}})$  is the redshift dependent Hubble parameter normalised to the reference redshift of the sample,  $z_{\text{ref}} = 0.2$ , and  $M_{\text{pivot}} = 10^{15} M_{\odot}$  is the pivot mass. The concentration at the reference mass and redshift is given by  $c_{200,\text{ref}} = 10^{\alpha_C}$ .

Statistical biases and correlation effects have to be carefully dealt with (Sereno et al. 2015b). For our analysis, we assume that both  $X = \text{Log}(M_{200}^M/M_{\text{pivot}})$ , that is, the covariate in Eq. (14), and  $Y = \text{Log}(c_{200})$ , that is, the response, are intrinsically scattered with respect to the true mass,  $Z$ , whose distribution we model as a Gaussian with redshift dependent mean and variance (Sereno & Ettori 2015a). We assume that the covariate is scattered but unbiased with respect to the true mass. We consider heteroscedastic and correlated uncertainties for mass and concentration. For central location and scale, we consider the bi-weight estimators (Beers et al. 1990).

We apply non-informative priors (Sereno & Ettori 2015a, 2017): the uniform distribution for  $\alpha_C$  and the mean of the distribution of  $Z$ ; the Student's  $t_1$  distribution with one degree of freedom for the slopes  $\beta_C$  and  $\gamma_C$ ; the Gamma distribution for the inverse of either variances or intrinsic scatters.

The regression favors a flattening and upturn of the relation at large masses, in agreement with theoretical predictions (Diemer & Joyce 2019). In particular, the best fit values of the linear relation are

$$\alpha_C = 0.49 \pm 0.07, \quad \beta_C = 0.20 \pm 0.31, \quad \gamma_C = -0.23 \pm 1.6. \quad (15)$$

To test the robustness of the results on the regression scheme, we also fit the relation with a simple linear model, similarly to

<sup>7</sup> The package LIRA (LInear Regression in Astronomy) is publicly available from the Comprehensive R Archive Network at <https://cran.r-project.org/web/packages/lira/index.html>.

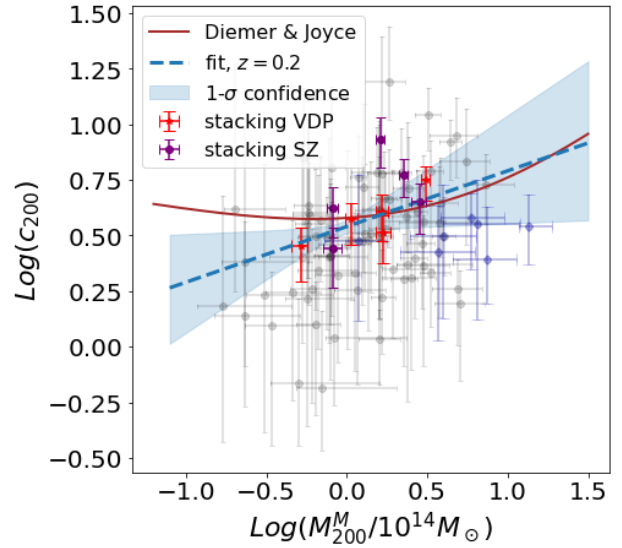


**Fig. 8.** Concentration-mass relation for the CHEXMATE sample. The errorbars indicates 68% uncertainties in the parameters; we highlighted in light blue the clusters with  $\text{Log}(M_{200}^M/M_{\sigma,200c}) > 0.3$ . The blue-dashed line is the best fit Bayesian linear regression derived with the method of Sereno & Ettori (2015b); the shaded region represents the corresponding  $1\sigma$  contour. Purple and red crosses indicates the values obtained by stacking clusters in bin of SZ mass and  $\sigma_{\text{ap},200}$ , as explained in Sect. 5. The brown solid line shows the theoretical prediction of Diemer & Joyce (2019).

that done, for instance in Biviano et al. (2017), using the ODR method and neglecting the redshift dependence,

$$\text{Log} c_{200} = A_1 \text{Log} \left( \frac{M_{200}^M}{10^{14} M_{\odot}} \right) + A_2. \quad (16)$$

We found  $A_1 = 0.27 \pm 0.08$ ,  $A_2 = 0.20 \pm 0.11$ , which confirms the trend of rising concentration for high mass clusters. The same is valid if we fit separately T1 and T2 clusters, in particular  $A_1^{T1} = 0.35 \pm 0.12$  and  $A_1^{T2} = 0.21 \pm 0.14$ . Our findings might appear to be in tension with other theoretical expectations (e.g., Dutton & Macciò 2014; Ragagnin et al. 2020) and observational determinations of the  $c - M$  relation (e.g., Merten et al. 2015; Biviano et al. 2017, where the latter is also based on the MG-MAMPOSST technique). However, this statement should be considered cautiously. The CHEX-MATE sample covers the very massive end of the halo mass function at intermediate redshifts, where the upturn is visible. Selection effects as well as the uncertainties in the kinematic play a significant role; in particular, X-ray and SZ-selected samples tend to favor more centrally concentrated and relaxed clusters, biasing the inferred  $c - M$  relation upward (e.g., Meneghetti et al. 2014). Moreover, as mentioned before, the presence of residual interlopers may affect the high-mass end of the sample, giving rise to the observed trend.

#### 4.3. Substructures and un-relaxation

To further investigate the overall kinematical state of the cluster sample, we compute the Anderson-Darling coefficient  $A^2$  (Anderson & Darling 1952), which measures deviation from Gaussianity of the LOS velocity distribution, which is a good indicator of the dynamical state of a cluster (e.g., Roberts et al. 2018).



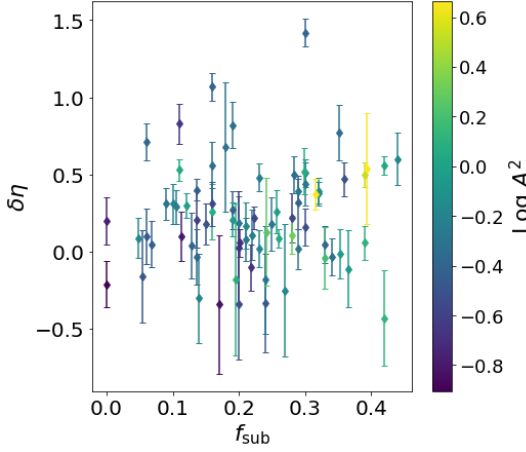


**Fig. 9.**  $\delta\eta = \text{Log } M_{500}^M - \text{Log } M_{500}^{SZ}$  as a function of the fraction of galaxies in substructures  $f_{\text{sub}}$ , computed using the DS+ code of Benavides et al. (2023). Colors and errorbars are as in Figure 7.

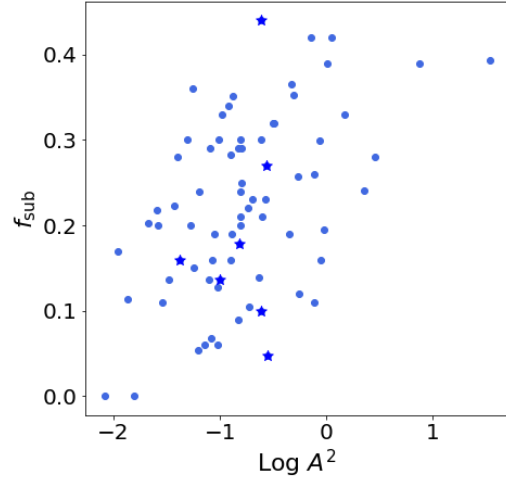


**Fig. 10.** Fraction of galaxies in substructures  $f_{\text{sub}}$  as a function of the logarithm of the Anderson-Darling coefficient  $A^2$ . The darker stars indicate the clusters for which  $\text{Log } (M_{200}^M / M_{\sigma,200c}) > 0.3$

Large values of  $A^2$  have been shown to be associated with deviations from relaxation (e.g., Pizzuti et al. 2020; Barrena et al. 2024). The colors of each point in Fig. 7 indicates the corresponding value of the (logarithm of the) Anderson-Darling coefficient, computed using all galaxies within  $R = r_{\text{ap},200c}$  as given by CLEAN (Serenio et al. 2025). No strong correlations can be highlighted among  $A^2$  and  $\delta\eta$ , but dividing again the sample into two subsamples according to the median value  $A^2 = 0.44$ , the average logarithmic differences in the two bins, computed by 1000 bootstrap resampling, are  $\langle \delta\eta \rangle = 0.23 \pm 0.08$  and  $0.13 \pm 0.07$  for  $A^2 > 0.44$  and  $A^2 < 0.44$ , respectively. This small difference in mean  $|\delta\eta|$  shows a weak preference of lower biases for clusters with a more regular LOS velocity dispersion.

The MG-MAMPOSST method may be sensitive to the presence of relevant substructures in clusters, which are connected to recent merging activity and thus indicate a possible disturbed dynamical state (e.g., Wen & Han 2013; Parekh et al. 2015; Kim-mig et al. 2023). Thus, we search for possible correlations between the number of substructures in the cluster and the observed logarithmic difference  $\delta\eta$ . We estimate the fraction of galaxies  $f_{\text{sub}}$  in substructures over the total number of galaxies within  $R = r_{200}$  by means of the DS+ method<sup>8</sup> of Benavides et al. (2023). This DS+ method extends the original algorithm of Dressler & Shectman (1988) for the identification of sub-groups in clusters by looking for galaxy clumps whose mean velocities and dispersion deviate from the global cluster values. DS+ employs a combination of projected position and line-of-sight velocities to identify substructures and estimate the probability of each galaxy of belonging to each of those groups.

For each cluster, we run 1000 Monte Carlo simulations and we set a p-value of 0.01 as threshold for the identification of a substructure (see also Barrena et al. 2024). We work in the so called non-overlapping mode, i.e., each galaxy is attributed to at most one group. We then define  $f_{\text{sub}} = N_{\text{sub}}/N_{200}$ , where  $N_{\text{sub}}$  is the total number of galaxies in all the substructures found by DS+, and  $N_{200}$  is the number of members in the projected cylinder  $R < r_{200}$ . In Figure 9, the distribution of  $\delta\eta$  as a function of  $f_{\text{sub}}$  is shown, color-coded according to the values of  $A^2$ . Again, no relevant trends can be drawn from the sample, with a more scattered distribution across the range of  $f_{\text{sub}}$ . It is worth pointing out that a  $\delta\eta$  close to zero does not indicate that the clus-

ter mass estimations are unbiased, but it may suggest that both SZ and kinematic masses are biased towards the same direction. Figure 10 further shows the relation between  $f_{\text{sub}}$  and  $\text{Log } A^2$ . It is evident that, despite the correlation not being strong (Pearson coefficient  $r = 0.43$ ), a trend of having large  $A^2$  for large values of  $f_{\text{sub}}$  is present.

A more accurate analysis would involve masses estimated from weak lensing (WL), as well as the combination of different morphological parameters (e.g., those derived from X-ray analyses, see Campitiello et al. 2022) to have a clearer indication of the equilibrium state of the clusters. This will be the subject of a follow-up work.

## 5. Orbits of galaxies as a function of mass and redshift

The orbital anisotropy of member galaxies in clusters is one of the key quantities in kinematic analyses. It has been shown that the nature of anisotropy can be linked to the dynamical state of the cluster and its formation history (e.g., Mamon et al. 2019); in general, studies of observed clusters and cluster-size halos in cosmological simulations have identified an overall trend of isotropic orbits in the cluster core, and an increasing radial anisotropy towards the outskirts. Moreover, galaxies of different morphological types in clusters exhibit different orbital behaviors. In particular, early-type galaxies which are expected to have fallen into the cluster at early times may prefer more isotropic orbits, while spiral galaxies are thought to follow fairly radial paths (e.g., Munari et al. 2014; Mamon et al. 2019; Biviano et al. 2024). The reconstruction of anisotropy profiles in clusters is generally a complicated issue; this is because  $\beta(r)$  is not a direct observable and it is degenerate with the total mass (Binney & Mamon 1982), constituting a possible source of systematic error in the reconstruction of dynamical mass profiles. To address this, both parametric approaches (e.g., Mamon et al. 2013; Read et al. 2021) and non-parametric methods (see e.g., Mamon et al. 2019 and references therein) have been developed. The MG-MAMPOSST technique (as does the original MAMPOSST) relies on a joint parametric modeling of both mass and anisotropy profiles, which has been shown to work robustly and adequately well in a wide range of cases (Mamon et al. 2013; Pizzuti et al. 2020; Biviano et al. 2023). However, the uncertainties in the re-

<sup>8</sup> The code is freely available at <https://github.com/josegit88/MilaDS>.

constructed radial profile  $\beta(r)$  are quite large for a single cluster, even for a considerably large number of members in the MG-MAMPOSST fit (see the example of PSZ2 G067.17+67.46 in the bottom plot of Figure 2, with  $N_{\text{gal}} = 299$  galaxies used in the analysis).

This issue can be solved in two ways. One possibility is to assume prior constraints on the mass profile, as provided, for example, by hydrostatic equilibrium or WL analyses (e.g., Annunziatella et al. 2016; Aguerri et al. 2017). On the other hand, one can infer information on the anisotropy profile as a function of cluster mass and redshift by populating the PPS with a stacking procedure. Here, we adopt the latter approach and perform two different stacking procedures. First, we identify clusters with similar velocity dispersions in two redshift bins, namely  $z \leq 0.2$  and  $0.2 < z < 0.6$  (which mostly splits clusters into the T1 or the T2 subsample). In the first bin, we further divide clusters in three sub-bins of velocity dispersion, centered on  $\sigma_{\text{ap},200}/[\text{km s}^{-1}] = 750, 980, 1360$ , respectively. We then generate the three stacked clusters (one for each bin of  $\sigma_{\text{ap},200}$ ) by considering all the member galaxies of CHEX-MATE clusters belonging to the same bin. The choices of the bins and the construction ensure that each stack contains  $N \sim 3000$  galaxies. For the high-redshift bin, we end up with only two stacked clusters, with  $\sigma_{\text{ap},200}/[\text{km s}^{-1}] = 1040, 1600$ .

The second stacking has been performed considering five bins for clusters with similar SZ-X-ray calibrated masses - three for  $z < 0.2$ ,  $M_{500}^{\text{SZ}}/10^{14} M_{\odot} = 3.23, 5.48, 7.74$ , and two for  $z > 0.2$ ,  $M_{500}^{\text{SZ}}/10^{14} M_{\odot} = 7.91, 12.10$ . This second set is to consider a stacking criterion ( $M_{500}^{\text{SZ}}$ ) which is independent from kinematic variables. As an example, the stacked PPS for this case are shown in Appendix C.

For each of the 10 stacked clusters, we consider galaxies in the projected range  $[0.05 \text{ Mpc}, 1.1 \langle r_{200,\text{ap}} \rangle]$ , where  $\langle r_{200,\text{ap}} \rangle$  is the average of  $r_{200,\text{ap}}$  over all the clusters in the bin. We apply the MG-MAMPOSST method assuming a NFW model for the mass distribution and a pNFW for the projected number density distribution; as before, we perform a MCMC sampling of the parameter space  $\{r_{200}, r_s, r_v, \mathcal{A}_0, \mathcal{A}_{\infty}\}$ , adopting the same flat prior listed in Sect. 3.

Fig. 11 and Fig. 12 show the radial profiles of the velocity anisotropy obtained from the MG-MAMPOSST analysis of the stacked clusters ( $\sigma_{\text{ap},200}$  and SZ, respectively) at  $z < 0.2$  (top panels in each plot) and  $z > 0.2$  (bottom panels in each plot). For the stacking in velocity dispersion, we see that all the profiles (except the one for the most massive cluster,  $\sigma_{\text{ap},200} \sim 1600 \text{ km s}^{-1}$ ) are consistent with central isotropic orbits within one  $\sigma$ , and with an increase of the anisotropy towards the cluster outskirts, as found by other studies in the literature (Mamon et al. 2019).

In the bottom right panel, we can observe a slight, although not very significant, trend to have more radial orbits at the virial radius for clusters with a larger velocity dispersion. The most massive stacked cluster exhibits a more 'extreme' behavior, passing from tangential orbits ( $\beta < 0$ ) at the center, to largely radial ones in the outskirts. However, this bin contains clusters with  $\delta\eta > 0.8$ , which, as we have discussed, are characterized by disturbed dynamical states.

The same trend of increasing radial orbits at virial radius is found in terms of the SZ mass, as highlighted in Fig. 12. In this case, however, only the first mass sub-bins in each redshift cut ( $z < 0.2$  and  $z > 0.2$ ) exhibit a central anisotropy consistent with zero at the 68% C.L., while the others are in agreement with no anisotropy at the 95% C.L., with a slight preference for central tangential orbits which is not very statistically significant.

## 6. Conclusions

In this paper we have studied the kinematical and dynamical properties of 75 massive galaxy clusters, as part of the CHEX-MATE sample, for which high-precision spectroscopic measurements of LOS velocities and projected positions are available. By means of the MG-MAMPOSST code, we have jointly reconstructed mass profiles and velocity anisotropy profiles for eight combinations of mass and number density models. We found that the NFW prescription is preferred by the kinematic analysis for about half of the sample, followed by the Burkert model. This confirms the assumptions of the halo model used in the dynamical mass determinations of Sereno et al. (2025). Moreover, the constraints on the virial radius  $r_{200}$  (and on the mass  $M_{200}$ ) are robust against variations in the mass and number density models, as shown by the relatively small systematic uncertainties (Table A.1).

We have compared the masses obtained from the SZ-X-ray calibrated signal, finding  $(1 - B_1) = 0.54 \pm 0.11$  when clusters with evident disturbed dynamical states are removed; a negligible bias is instead obtained while fitting with a linear relation allowing for mass dependence,  $(1 - B) = 1.04 \pm 0.09$ . When also the clusters with a logarithmic mass difference  $\delta\eta > 0.8$  dex (which are high-velocity dispersions  $\sigma_{\text{ap},200} > 1.4 \times 10^3 \text{ km/s}$ ) are considered, an overall positive mass-dependent bias  $(1 - B) = 0.67$  is found. Note that SZ masses may be overestimated due to the Malmquist bias, as discussed in Sereno et al. (2025); this might affect our findings producing a larger value of  $(1 - B)$ . A refined analysis is however beyond the scope of the current work, as it has already been performed in Sereno et al. (2025). The concentration-mass relation has been further investigated and compared to theoretical expectations. By performing a Bayesian linear regression by means of the LIRA package, we found a slight evidence of a rising trend at large masses, as also predicted by the model of Diemer & Joyce (2019). Interestingly, the results obtained for the sample of CHEX-MATE clusters are fully consistent with the prediction of the  $\Lambda$ CDM scenario, given an average value of  $\langle c_{200} \rangle = 3.5$  with a scatter of 1.8. The results of the various scaling relations investigated in this work are summarized in Table 1.

The dynamical state of the clusters has been studied by comparing  $\delta\eta$  with two quantities that can be related with dynamical un-relaxation and disturbed morphology, namely the Anderson-Darling coefficient  $A^2$  and the fraction of galaxies in substructures  $f_{\text{sub}}$ . No evident relations have been found for  $A^2$  and  $f_{\text{sub}}$ . Nevertheless, a lower averaged  $\delta\eta$  is obtained for clusters with  $A^2 < 0.44$  (being 0.44 the median value of the sample). Note however that a more complete analysis should investigate the differences with the weak lensing mass determinations as well as account for the X-ray morphology to better identify substructures and departures from equilibrium. This will be the subject of an upcoming work.

Finally, the shape of the radial velocity anisotropy profile has been studied by dividing the sample in two bins of redshift, and first collecting clusters within three and two sub-bins of  $\sigma_{\text{ap},200}$ , respectively. We stacked clusters in the same bin and applied MG-MAMPOSST to those stacked systems to reconstruct the orbits from the center to the edges. We performed a similar stacking procedure considering bins of  $M_{500}^{\text{SZ}}$ , which are not directly related to the kinematical properties of the clusters. Consistent with the literature, orbits tend to be isotropic or tangential at the center and more radial towards the edge of the clusters, where galaxies are thought to be falling in the cluster's potential for the first time (Mamon et al. 2019). There is a slight trend towards in-

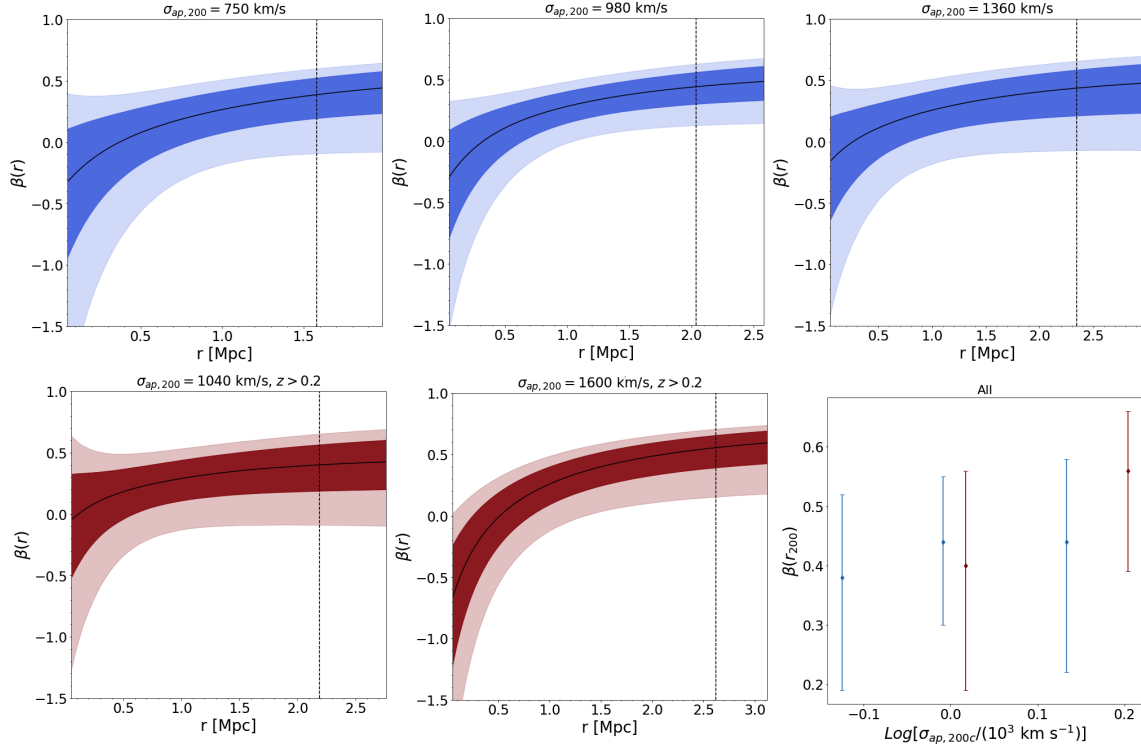


**Fig. 11.** Radial velocity anisotropy profiles for stacked clusters, where the stacking is in velocity dispersion. The bands show the 68% and 95% regions, while the black curve is the median profile. Top:  $z < 0.2$ . Bottom:  $z > 0.2$ . The bottom right plot shows the value of  $\beta(r = r_{200})$  with 68% errorbars (blue and red for  $z < 0.2$  and  $z > 0.2$ , respectively).

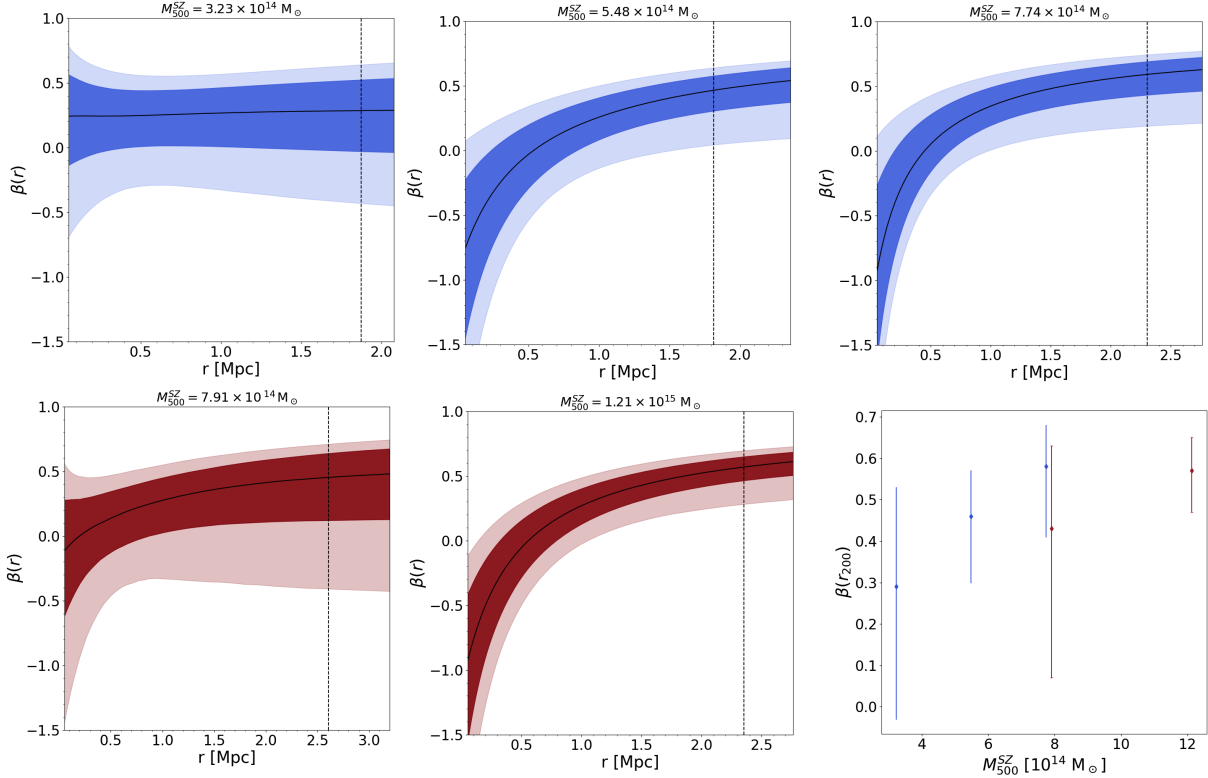


**Fig. 12.** Radial velocity anisotropy profiles for the stacked clusters, where the stacking is in bins of  $M_{500}^{SZ}$ . The structure is exactly as in Fig. 11.

**Table 1.** Summary of the results for the parameters of the linear fits of the relations discussed in this paper.

Relation	reference	constraints
$\text{Log } M_{200}^M - \sigma_{\text{ap},200}$	Eq. (9)	$\alpha_\sigma = 3.61 \pm 0.17, \beta_\sigma = 1.07 \pm 0.01, \gamma_\sigma = -0.83 \pm 0.70$
$\text{Log } M_{500}^M - \text{Log } M_{500}^{SZ}$ (outliers removed)	Eq. (12) $\alpha_{SZ}$ fixed to 1	$\alpha_{SZ} = 0.71 \pm 0.04, 1 - B = 1.04 \pm 0.09$ $(1 - B_1) = 0.54 \pm 0.11$
$\text{Log } c_{200} - \text{Log } M_{200}^M$ (outliers removed)	Eq. (14)	$\alpha_C = 0.49 \pm 0.07, \beta_C = 0.20 \pm 0.31, \gamma_C = -0.23 \pm 1.6$

creasingly radial orbits at  $r_{200}$  with larger  $\sigma_{\text{ap},200}$  (which, in turn, is connected to larger dynamical masses); we found the same trend with increasing  $M_{500}^{SZ}$ .

More broadly, our results indicate that the most massive galaxy clusters at  $z < 0.6$  are generally close to dynamical equilibrium. Nonetheless, we identify some cases where even the most massive systems appear to deviate from full virialisation. As previously mentioned, a comprehensive assessment of the dynamical state of the CHEX-MATE sample will be carried out in a forthcoming study, which will incorporate a more complete set of morphological and kinematic indicators, as well as a comparison with mass estimates from weak lensing and X-ray data.

**Acknowledgements.** This project has been partially funded by the Spanish Ministerio de Ciencia, Innovación y Universidades through the programme Generación del Conocimiento 2021, with code PID2021-122665OB-I00. R. Barrena acknowledges support by the Severo Ochoa 2020 research programme of the Instituto de Astrofísica de Canarias. S.E., M.S., acknowledge the financial contribution from the contracts Prin-MUR 2022 supported by Next Generation EU (M4.C2.1.1, n.20227RNLY3 *The concordance cosmological model: stress-tests with galaxy clusters*). M.S. acknowledges financial contributions from INAF Theory Grant 2023: Gravitational lensing detection of matter distribution at galaxy cluster boundaries and beyond (1.05.23.06.17). S.E. acknowledges the financial contribution from the European Union's Horizon 2020 Programme under the AHEAD2020 project (grant agreement n. 871158). DE acknowledges support from the Swiss National Science Foundation (SNSF) through grant agreement 200021\_212576. C.P.H. acknowledges support from ANID through Fondecyt Regular project number 1252233. JS was supported by NASA Astrophysics Data Analysis Program (ADAP) Grant 80NSSC21K1571. BJM acknowledges support from Science and Technology Facilities Council grants ST/V000454/1 and ST/Y002008/1. GWP acknowledges long-term support from CNES, the French space agency. GC acknowledges the support from the Next Generation EU funds within the National Recovery and Resilience Plan (PNRR), Mission 4 - Education and Research, Component 2 - From Research to Business (M4C2), Investment Line 3.1 - Strengthening and creation of Research Infrastructures, Project IR0000012 - "CTA+ - Cherenkov Telescope Array Plus". MD acknowledges the support of two NASA programs: NASA award 80NSSC19K0116/SAO subaward SV9-89010 and NASA award 80NSSC 22K0476.

## References

Abell, G. O. 1958, *ApJS*, 3, 211  
Aguado-Barahona, A., Rubiño-Martín, J. A., Ferragamo, A., et al. 2022, *A&A*, 659, A126  
Aguerri, J. A. L., Agullí, I., Diaferio, A., & Dalla Vecchia, C. 2017, *MNRAS*, 468, 364  
Amodeo, S., Mei, S., Stanford, S. A., et al. 2017, *ApJ*, 844, 101  
Anderson, T. W. & Darling, D. A. 1952, *The Annals of Mathematical Statistics*, 23, 193  
Annunziatella, M., Mercurio, A., Biviano, A., et al. 2016, *A&A*, 585, A160  
Barrena, R., Pizzuti, L., Chon, G., & Böhringer, H. 2024, *A&A*, 691, A135  
Beers, T. C., Flynn, K., & Gebhardt, K. 1990, *AJ*, 100, 32  
Benavides, J. A., Biviano, A., & Abadi, M. G. 2023, *A&A*, 669, A147  
Binney, J. & Mamon, G. A. 1982, *MNRAS*, 200, 361  
Biviano, A. & Katgert, P. 2004, *A&A*, 424, 779  
Biviano, A., Moretti, A., Paccagnella, A., et al. 2017, *A&A*, 607, A81  
Biviano, A., Pizzuti, L., Mercurio, A., et al. 2023, *Astrophys. J.*, 958, 148  
Biviano, A., Poggianti, B. M., Jaffé, Y., et al. 2024, *ApJ*, 965, 117  
Burkert, A. 1995, *ApJ*, 447, L25  
Campitiello, M. G., Ettori, S., Lovisari, L., et al. 2022, *A&A*, 665, A117  
Carlberg, R. G., Yee, H. K. C., & Ellingson, E. 1997, *ApJ*, 478, 462

Cavaliere, A. & Fusco-Femiano, R. 1981, *A&A*, 100, 194  
CHEX-MATE Collaboration, Arnaud, M., Ettori, S., et al. 2021, *A&A*, 650, A104  
Diemer, B. & Joyce, M. 2019, *ApJ*, 871, 168  
Dressler, A. & Shectman, S. A. 1988, *AJ*, 95, 985  
Dutton, A. A. & Macciò, A. V. 2014, *MNRAS*, 441, 3359–3374  
Einasto, J. 1965, *Trudy Astrofizicheskogo Instituta Alma-Ata*, 5, 87  
Ettori, S., Donnarumma, A., Pointecouteau, E., et al. 2013, *Space Sci. Rev.*, 177, 119  
Ferragamo, A., Barrena, R., Rubiño-Martín, J. A., et al. 2021, *A&A*, 655, A115  
Ferragamo, A., Rubiño-Martín, J. A., Betancort-Rijo, J., et al. 2020, *A&A*, 641, A41  
Gelman, A. & Rubin, D. B. 1992, *Statistical Science*, 7, 457  
Hernquist, L. 1990, *ApJ*, 356, 359  
Kimmig, L. C., Remus, R.-S., Dolag, K., & Biffi, V. 2023, *ApJ*, 949, 92  
Kravtsov, A. V., Vikhlinin, A., & Nagai, D. 2006, *ApJ*, 650, 128  
Lesci, G. F., Veropalumbo, A., Sereno, M., et al. 2023, *A&A*, 674, A80  
Lotz, M., Remus, R.-S., Dolag, K., Biviano, A., & Burkert, A. 2019, *MNRAS*, 488, 5370  
Macciò, A. V., Dutton, A. A., & van den Bosch, F. C. 2008, *MNRAS*, 391, 1940  
Mamon, G. A., Biviano, A., & Boué, G. 2013, *MNRAS*, 429, 3079  
Mamon, G. A., Biviano, A., & Murante, G. 2010, *A&A*, 520, A30  
Mamon, G. A., Cava, A., Biviano, A., et al. 2019, *A&A*, 631, A131  
Meneghetti, M., Rasia, E., Vega, J., Merten, J., & Postman, M. e. a. 2014, *ApJ*, 797, 34  
Merten, J., Meneghetti, M., Postman, M., et al. 2015, *ApJ*, 806, 4  
Munari, E., Biviano, A., Borgani, S., Murante, G., & Fabjan, D. 2013, *MNRAS*, 430, 2638  
Munari, E., Biviano, A., & Mamon, G. A. 2014, *A&A*, 566, A68  
Navarro, J. F., Frenk, C. S., & White, S. D. M. 1997, *ApJ*, 490, 493  
Parekh, V., van der Heyden, K., Ferrari, C., Angus, G., & Holwerda, B. 2015, *A&A*, 575, A127  
Penna-Lima, M., Bartlett, J. G., Roza, E., et al. 2017, *A&A*, 604, A89  
Pizzuti, L., Boumechta, Y., Haridasu, S., et al. 2024, *Journal of Cosmology and Astroparticle Physics*, 2024, 014  
Pizzuti, L., Saltas, I. D., & Amendola, L. 2021, *MNRAS*, 506, 595  
Pizzuti, L., Saltas, I. D., Biviano, A., Mamon, G., & Amendola, L. 2023, *JOSS*, 8, 4800  
Pizzuti, L., Sartoris, B., Borgani, S., & Biviano, A. 2020, *JCAP*, 04, 024  
Planck Collaboration, Aghanim, N., Akrami, Y., et al. 2020, *A&A*, 641, A6  
Pratt, G. W., Arnaud, M., Biviano, A., et al. 2019, *Space Sci. Rev.*, 215, 25  
Ragagnin, A., Saro, A., Singh, P., & Dolag, K. 2020, *MNRAS*, 500, 5056–5071  
Read, J. I., Mamon, G. A., Vasiliev, E., et al. 2021, *MNRAS*, 501, 978  
Roberts, I. D., Parker, L. C., & Hlavacek-Larrondo, J. 2018, *MNRAS*, 475, 4704  
Ruel, J., Bazin, G., Bayliss, M., et al. 2014, *ApJ*, 792, 45  
Sarazin, C. L. 1980, *ApJ*, 236, 75  
Sereno, M. 2016, *MNRAS*, 455, 2149  
Sereno, M. & Ettori, S. 2015a, *MNRAS*, 450, 3675, (CoMaLit-IV)  
Sereno, M. & Ettori, S. 2015b, *MNRAS*, 450, 3633, (CoMaLit-I)  
Sereno, M. & Ettori, S. 2017, *MNRAS*, 468, 3322, (CoMaLit-V)  
Sereno, M., Ettori, S., & Moscardini, L. 2015a, *MNRAS*, 450, 3649, (CoMaLit-II)  
Sereno, M., Giocoli, C., Ettori, S., & Moscardini, L. 2015b, *MNRAS*, 449, 2024  
Sereno, M., Maurogordato, S., Cappi, A., et al. 2025, *A&A*, 693, A2  
Sunyaev, R. A. & Zeldovich, Y. B. 1972, *Comments on Astrophysics and Space Physics*, 4, 173  
Tiret, O., Combes, F., Angus, G. W., Famaey, B., & Zhao, H. S. 2007, *A&A*, 476, L1  
Tonnesen, S. 2019, *ApJ*, 874, 161  
van der Burg, R. F. J., Muzzin, A., & Hoekstra, H. 2016, *A&A*, 590, A20  
Wen, Z. L. & Han, J. L. 2013, *MNRAS*, 436, 275–293  
Zarattini, S., Biviano, A., Aguerri, J. A. L., Girardi, M., & D’Onghia, E. 2021, *A&A*, 655, A103  
Zwicky, F. 1933, *Helvetica Physica Acta*, 6, 110



## Appendix A: Results from MG-MAMPOSST

The constraints on the mass profile, number density and velocity anisotropy parameters are summarized in Table A.1, along with cluster redshift, Anderson-Darling coefficient  $A^2$ , fraction of galaxies in substructures  $f_{\text{sub}}$ , number of galaxies  $N_{200}$  within a projected cylinder  $R < r_{\text{ap},200}$  aperture velocity dispersion. Here we included also the MG-MAMPOSST analysis of clusters PSZ2G113.91-37.01 and PSZ2G083.29-31.03, which have less than  $N = 50$  members within  $r_{200,\text{ap}}$ .

## Appendix B: Disturbed clusters

Here we show the projected phase space, the histogram of the line of sight velocities and the two-dimensional spatial distribution for the four clusters characterized by a value of  $\delta\eta > 0.8$ , to highlight the evident disturbed dynamical state.

## Appendix C: Stacked projected-phase-spaces for in bins of $M_{500}^{\text{SZ}}$

. In Figure C.1 we plot the PPS of the five stacked clusters obtained by collecting member galaxies in bins of SZ masses, for Tier 1 (top plots, blue points) and Tier 2 (bottom plots, green points).

## Appendix D: GTC clusters data

Here we report an extract of the member galaxies with measured spectroscopic redshifts for the three clusters observed with the OSIRIS spectrograph at the GTC. These three catalogues are organised as follow: first column corresponds to an ID label; the second and third columns indicate the right ascension and declination coordinates in J2000 epoch (RA and Dec); the fourth is the measured redshift and the last column is the errors on the redshift. The full catalogues are available upon request to the authors.

**Table A.1.** Constraints on the free parameters from the kinematic analysis with MG-MAMPOSSt, shown for the combination of mass and number density model which provides the best BIC.

PSZ2 name	Mass	$N(R)$	$r_{200}$ [Mpc]	$r_v$ [Mpc]	$r_s$ [Mpc]	$\mathcal{A}_\infty$	$\mathcal{A}_0$	$-\ln P$	$z$	$A^2$	$f_{\text{sub}}$	$N_{200}$	$\sigma_{\text{ap},200}$ [km/s]
G049.22+30.87	NFW	pNFW	$2.13^{+0.25}_{-0.27} \pm 0.06$	$0.59^{+0.10}_{-0.13} \pm 0.28$	$0.81^{+1.22}_{-0.72} \pm 0.73$	$1.42^{+1.76}_{-0.93} \pm 0.09$	$1.78^{+2.36}_{-1.33} \pm 0.10$	3403.919	0.1606	0.27	0.29	368	1034.0
G226.18+76.79	Bur	pHer	$2.29^{+0.53}_{-0.44} \pm 0.04$	$0.67^{+0.17}_{-0.13} \pm 0.24$	$0.30^{+0.41}_{-0.28} \pm 0.38$	$1.64^{+1.94}_{-1.18} \pm 0.04$	$1.46^{+2.71}_{-1.00} \pm 0.14$	1171.266	0.1415	0.44	0.09	131	1069.0
G053.53+59.52	NFW	pHer	$2.40^{+0.36}_{-0.32} \pm 0.08$	$0.87^{+0.14}_{-0.15} \pm 0.30$	$0.85^{+1.21}_{-0.73} \pm 0.66$	$1.58^{+1.90}_{-1.10} \pm 0.12$	$1.33^{+2.16}_{-0.89} \pm 0.16$	2100.914	0.1136	0.78	0.12	222	1056.0
G056.77+36.32	NFW	pNFW	$3.41^{+0.81}_{-0.76} \pm 0.15$	$0.85^{+0.29}_{-0.16} \pm 0.74$	$2.09^{+1.64}_{-1.54} \pm 0.46$	$1.38^{+2.14}_{-0.91} \pm 0.14$	$1.17^{+2.42}_{-0.70} \pm 0.39$	981.519	0.09696	0.41	0.19	96	1364.0
G042.81+56.61	NFW	pNFW	$2.48^{+0.31}_{-0.29} \pm 0.08$	$0.53^{+0.17}_{-0.15} \pm 0.49$	$0.63^{+0.76}_{-0.52} \pm 0.77$	$1.63^{+1.78}_{-1.06} \pm 0.08$	$1.44^{+2.38}_{-1.00} \pm 0.10$	2014.210	0.07225	0.54	0.30	210	1168.0
G033.81+77.18	Bur	pNFW	$1.79^{+0.31}_{-0.25} \pm 0.05$	$0.34^{+0.12}_{-0.12} \pm 0.34$	$0.40^{+0.56}_{-0.37} \pm 0.61$	$1.48^{+1.82}_{-1.01} \pm 0.08$	$2.09^{+2.38}_{-1.60} \pm 0.17$	1293.172	0.06272	0.56	0.23	154	818.0
G041.45+29.10	Bur	pHer	$2.40^{+0.52}_{-0.44} \pm 0.15$	$0.38^{+0.10}_{-0.08} \pm 0.14$	$0.12^{+0.15}_{-0.08} \pm 0.15$	$1.74^{+1.78}_{-1.22} \pm 0.09$	$1.77^{+2.46}_{-1.32} \pm 0.10$	961.440	0.1771	0.28	0.37	110	1332.0
G238.69+63.26	Her	pHer	$1.83^{+0.28}_{-0.26} \pm 0.07$	$1.95^{+0.20}_{-0.29} \pm 0.52$	$1.56^{+1.74}_{-1.30} \pm 0.46$	$1.51^{+2.00}_{-1.05} \pm 0.08$	$1.22^{+2.32}_{-0.76} \pm 0.16$	1770.555	0.1672	0.45	0.21	229	897.1
G080.41-33.24	NFW	pHer	$2.13^{+0.62}_{-0.55} \pm 0.18$	$0.36^{+0.08}_{-0.08} \pm 0.14$	$0.99^{+1.81}_{-0.97} \pm 0.69$	$1.34^{+1.74}_{-0.89} \pm 0.11$	$2.13^{+2.34}_{-1.62} \pm 0.09$	1124.055	0.1101	0.54	0.10	137	801.8
G048.10+57.16	Bur	pHer	$1.87^{+0.36}_{-0.33} \pm 0.06$	$1.11^{+0.24}_{-0.15} \pm 0.50$	$0.64^{+1.10}_{-0.63} \pm 0.73$	$1.49^{+1.84}_{-1.03} \pm 0.09$	$2.00^{+2.38}_{-1.54} \pm 0.10$	1546.255	0.07782	0.48	0.22	165	823.7
G287.46+81.12	Eis	pHer	$1.69^{+0.31}_{-0.29} \pm 0.06$	$1.72^{+0.36}_{-0.46} \pm 0.50$	$0.64^{+1.47}_{-0.64} \pm 0.73$	$1.85^{+1.83}_{-1.32} \pm 0.09$	$1.96^{+2.42}_{-1.50} \pm 0.10$	964.668	0.07194	0.25	0.28	109	832.7
G031.93+78.71	Bur	pNFW	$1.28^{+0.56}_{-0.73} \pm 0.06$	$0.35^{+0.31}_{-0.18} \pm 0.50$	$0.82^{+1.33}_{-0.82} \pm 0.73$	$1.76^{+1.85}_{-1.27} \pm 0.09$	$2.14^{+2.35}_{-1.63} \pm 0.10$	400.254	0.07533	0.28	0.20	57	589.5
G067.17+67.46	NFW	pNFW	$2.19^{+0.28}_{-0.29} \pm 0.06$	$0.74^{+0.20}_{-0.19} \pm 0.50$	$0.85^{+1.34}_{-0.75} \pm 0.73$	$1.55^{+1.72}_{-1.01} \pm 0.09$	$1.65^{+2.56}_{-1.20} \pm 0.10$	2880.857	0.1667	1.57	0.28	291	1057.0
G006.49+50.56	NFW	pNFW	$2.13^{+0.16}_{-0.15} \pm 0.06$	$1.08^{+0.19}_{-0.14} \pm 0.50$	$0.40^{+0.35}_{-0.27} \pm 0.73$	$2.02^{+1.58}_{-1.08} \pm 0.09$	$1.04^{+1.19}_{-0.58} \pm 0.10$	6711.942	0.07854	0.89	0.26	750	1066.0
G124.20-36.48	Her	pHer	$2.61^{+0.39}_{-0.37} \pm 0.06$	$1.22^{+0.11}_{-0.15} \pm 0.50$	$1.23^{+1.65}_{-1.10} \pm 0.73$	$1.55^{+1.86}_{-1.08} \pm 0.09$	$1.71^{+2.45}_{-1.26} \pm 0.10$	2031.290	0.1921	0.45	0.35	232	1282.0
G021.10+33.24	Eis	pNFW	$2.34^{+0.52}_{-0.75} \pm 0.06$	$1.79^{+1.38}_{-0.98} \pm 0.50$	$0.70^{+2.01}_{-0.68} \pm 0.73$	$1.59^{+2.05}_{-1.12} \pm 0.09$	$2.08^{+2.42}_{-1.63} \pm 0.10$	643.999	0.1511	0.95	0.08	74	1296.0
G044.20+48.66	NFW	pHer	$2.38^{+0.26}_{-0.28} \pm 0.06$	$2.33^{+0.14}_{-0.21} \pm 0.50$	$1.60^{+1.59}_{-1.20} \pm 0.73$	$1.42^{+1.74}_{-0.88} \pm 0.09$	$1.53^{+2.16}_{-0.99} \pm 0.10$	7619.565	0.08987	0.44	0.33	778	1090.0
G075.71+13.51	Her	pHer	$3.97^{+0.88}_{-0.85} \pm 0.06$	$0.50^{+0.13}_{-0.11} \pm 0.50$	$1.64^{+1.47}_{-1.18} \pm 0.73$	$1.26^{+1.95}_{-0.79} \pm 0.09$	$1.63^{+2.47}_{-1.19} \pm 0.10$	1249.919	0.05455	0.21	0.12	134	1723.0
G324.04+48.79	Eis	pHer	$1.79^{+0.48}_{-0.42} \pm 0.06$	$0.92^{+0.42}_{-0.29} \pm 0.50$	$0.97^{+2.04}_{-0.98} \pm 0.73$	$1.61^{+1.95}_{-1.14} \pm 0.09$	$1.96^{+2.33}_{-1.51} \pm 0.10$	634.364	0.4505	0.12	0.00	78	939.7
G284.41+52.45	NFW	pHer	$2.07^{+0.23}_{-0.26} \pm 0.04$	$2.19^{+0.40}_{-0.45} \pm 0.24$	$0.90^{+1.56}_{-0.89} \pm 0.38$	$1.49^{+1.52}_{-0.85} \pm 0.04$	$2.08^{+2.27}_{-1.52} \pm 0.14$	2983.187	0.4399	0.40	0.33	333	1247.0
G349.46-59.95	NFW	pHer	$3.46^{+1.16}_{-1.09} \pm 0.04$	$0.62^{+0.27}_{-0.22} \pm 0.24$	$1.35^{+1.92}_{-1.34} \pm 0.38$	$1.31^{+1.87}_{-0.85} \pm 0.04$	$2.35^{+2.27}_{-1.71} \pm 0.14$	719.670	0.3465	0.54	0.19	81	1591.0
G008.94-81.22	Bur	pHer	$3.05^{+0.32}_{-0.30} \pm 0.04$	$0.90^{+0.09}_{-0.06} \pm 0.24$	$0.26^{+0.18}_{-0.17} \pm 0.38$	$2.24^{+1.62}_{-1.41} \pm 0.04$	$1.17^{+1.96}_{-0.73} \pm 0.14$	4631.269	0.3064	0.87	0.39	491	1763.0
G266.04-21.25	NFW	pHer	$2.98^{+0.92}_{-0.83} \pm 0.04$	$0.46^{+0.10}_{-0.12} \pm 0.24$	$1.25^{+1.90}_{-1.21} \pm 0.38$	$1.43^{+1.85}_{-0.98} \pm 0.04$	$1.95^{+2.35}_{-1.50} \pm 0.14$	838.472	0.2965	0.25	0.15	93	1275.0

PSZ2 name	Mass	$N(R)$	$r_{200}$ [Mpc]	$r_v$ [Mpc]	$r_s$ [Mpc]	$\mathcal{A}_\infty$	$\mathcal{A}_0$	$-\ln P$	$z$	$A^2$	$f_{\text{sub}}$	$N_{200}$	$\sigma_{\text{ap},200}$ [km/s]
G107.10+65.32	Bur	pHer	$3.00^{+0.34}_{-0.32} \pm 0.04$	$1.74^{+0.10}_{-0.15} \pm 0.24$	$0.69^{+0.67}_{-0.51} \pm 0.38$	$1.62^{+1.92}_{-1.14} \pm 0.04$	$1.38^{+2.33}_{-0.93} \pm 0.14$	3463.596	0.2772	1.05	0.41	348	1491.0
G340.36+60.58	Eis	pHer	$2.84^{+0.42}_{-0.49} \pm 0.04$	$3.56^{+0.62}_{-0.73} \pm 0.24$	$1.53^{+1.77}_{-1.17} \pm 0.38$	$1.16^{+1.73}_{-0.69} \pm 0.04$	$1.72^{+2.47}_{-1.26} \pm 0.14$	3070.106	0.251	2.38	0.38	368	1426.0
G072.62+41.46	NFW	pHer	$2.52^{+0.33}_{-0.33} \pm 0.04$	$2.13^{+0.42}_{-0.34} \pm 0.24$	$1.54^{+1.81}_{-1.39} \pm 0.38$	$1.23^{+1.55}_{-0.72} \pm 0.04$	$2.11^{+2.30}_{-1.44} \pm 0.14$	3316.267	0.2255	0.34	0.19	368	1260.0
G055.59+31.85	NFW	pHer	$2.03^{+0.51}_{-0.50} \pm 0.04$	$3.74^{+1.12}_{-1.28} \pm 0.24$	$1.44^{+1.90}_{-1.36} \pm 0.38$	$1.55^{+1.94}_{-1.09} \pm 0.04$	$1.38^{+2.68}_{-0.93} \pm 0.14$	1095.847	0.2255	0.37	0.21	126	1056.0
G159.91-73.50	Eis	pHer	$2.70^{+0.31}_{-0.29} \pm 0.08$	$1.59^{+0.32}_{-0.27} \pm 0.30$	$0.74^{+0.78}_{-0.57} \pm 0.66$	$1.74^{+1.91}_{-1.28} \pm 0.12$	$1.04^{+2.12}_{-0.56} \pm 0.16$	2603.277	0.2095	1.19	0.36	272	1370.0
G195.75-24.32	NFW	pHer	$2.15^{+0.33}_{-0.30} \pm 0.08$	$1.32^{+0.24}_{-0.29} \pm 0.30$	$0.98^{+1.74}_{-0.99} \pm 0.66$	$1.49^{+1.84}_{-1.02} \pm 0.12$	$1.79^{+2.37}_{-1.34} \pm 0.16$	1430.192	0.2007	0.60	0.32	153	1043.0
G313.33+61.13	Eis	pHer	$2.87^{+0.36}_{-0.32} \pm 0.08$	$0.93^{+0.12}_{-0.09} \pm 0.30$	$0.28^{+0.20}_{-0.18} \pm 0.66$	$2.24^{+1.62}_{-1.40} \pm 0.12$	$1.16^{+1.74}_{-0.71} \pm 0.16$	4277.167	0.1848	1.00	0.40	492	1669.0
G208.80-30.67	Bur	pHer	$2.78^{+1.09}_{-0.76} \pm 0.08$	$0.83^{+0.31}_{-0.26} \pm 0.30$	$0.68^{+1.46}_{-0.65} \pm 0.66$	$1.61^{+1.93}_{-1.15} \pm 0.12$	$1.44^{+2.52}_{-0.98} \pm 0.16$	1141.373	0.2468	0.89	0.27	130	1242.0
G172.98-53.55	NFW	pHer	$3.08^{+0.77}_{-0.67} \pm 0.08$	$0.24^{+0.03}_{-0.03} \pm 0.30$	$0.39^{+0.45}_{-0.32} \pm 0.66$	$1.41^{+1.96}_{-0.95} \pm 0.12$	$1.48^{+2.47}_{-1.03} \pm 0.16$	2412.888	0.374	0.44	0.36	272	1682.0
G205.93-39.46	NFW	pNFW	$2.57^{+0.69}_{-0.62} \pm 0.08$	$0.57^{+0.46}_{-0.28} \pm 0.30$	$1.48^{+1.91}_{-1.43} \pm 0.66$	$1.33^{+1.85}_{-0.87} \pm 0.12$	$1.99^{+2.42}_{-1.52} \pm 0.16$	544.822	0.4409	0.36	0.07	65	1404.0
G273.59+63.27	Bur	pHer	$2.63^{+0.35}_{-0.33} \pm 0.15$	$1.74^{+0.48}_{-0.34} \pm 0.74$	$0.49^{+0.43}_{-0.33} \pm 0.46$	$2.08^{+1.71}_{-1.42} \pm 0.14$	$0.96^{+1.21}_{-0.49} \pm 0.39$	1685.399	0.1335	0.44	0.19	180	1288.0
G057.61+34.93	NFW	pHer	$2.19^{+0.35}_{-0.32} \pm 0.15$	$1.13^{+0.28}_{-0.28} \pm 0.74$	$0.62^{+1.30}_{-0.62} \pm 0.46$	$1.52^{+1.73}_{-0.98} \pm 0.14$	$1.93^{+2.41}_{-1.47} \pm 0.39$	1232.084	0.08492	0.50	0.22	141	1021.0
G046.88+56.48	NFW	pHer	$2.34^{+0.47}_{-0.43} \pm 0.15$	$2.69^{+0.80}_{-0.54} \pm 0.74$	$2.29^{+1.46}_{-1.36} \pm 0.46$	$1.60^{+1.96}_{-1.13} \pm 0.14$	$0.84^{+0.54}_{-0.36} \pm 0.39$	1834.999	0.1137	0.61	0.27	204	1087.0
G243.64+67.74	Bur	pNFW	$1.41^{+0.56}_{-0.86} \pm 0.15$	$0.61^{+0.43}_{-0.25} \pm 0.74$	$0.84^{+1.52}_{-0.84} \pm 0.46$	$1.61^{+1.96}_{-1.15} \pm 0.14$	$2.30^{+2.33}_{-1.81} \pm 0.39$	488.051	0.08108	0.55	0.30	54	696.2
G008.31-64.74	NFW	pHer	$4.43^{+0.57}_{-0.61} \pm 0.15$	$0.68^{+0.11}_{-0.12} \pm 0.74$	$1.39^{+1.14}_{-0.98} \pm 0.46$	$1.04^{+1.80}_{-0.57} \pm 0.14$	$1.85^{+2.43}_{-1.33} \pm 0.39$	2369.679	0.3153	0.57	0.26	249	1978.0
G285.63+72.75	Eis	pHer	$2.12^{+0.36}_{-0.33} \pm 0.15$	$1.36^{+0.33}_{-0.36} \pm 0.74$	$0.95^{+1.78}_{-0.89} \pm 0.46$	$1.58^{+1.95}_{-1.12} \pm 0.14$	$1.74^{+2.48}_{-1.29} \pm 0.39$	1243.294	0.1667	0.34	0.14	140	995.7
G077.90-26.63	Bur	pNFW	$1.86^{+0.61}_{-0.88} \pm 0.08$	$0.45^{+0.24}_{-0.15} \pm 0.49$	$0.73^{+1.60}_{-0.73} \pm 0.77$	$1.71^{+1.83}_{-1.24} \pm 0.08$	$2.29^{+2.28}_{-1.78} \pm 0.10$	725.684	0.1449	0.29	0.14	81	915.0
G114.79-33.71	NFW	pNFW	$2.06^{+0.37}_{-0.34} \pm 0.08$	$0.44^{+0.19}_{-0.14} \pm 0.49$	$0.87^{+1.51}_{-0.80} \pm 0.77$	$1.49^{+1.87}_{-1.02} \pm 0.08$	$1.64^{+2.49}_{-1.19} \pm 0.10$	1316.109	0.09447	0.20	0.21	155	953.6
G224.00+69.33	NFW	pHer	$2.28^{+0.50}_{-0.44} \pm 0.05$	$0.96^{+0.31}_{-0.24} \pm 0.34$	$0.88^{+1.96}_{-0.88} \pm 0.61$	$1.45^{+1.88}_{-0.99} \pm 0.08$	$2.06^{+2.36}_{-1.58} \pm 0.17$	983.873	0.1917	0.35	0.20	114	1078.0
G113.91-37.01	Eis	pHer	$2.87^{+1.07}_{-0.96} \pm 0.05$	$0.59^{+0.13}_{-0.17} \pm 0.34$	$1.15^{+1.97}_{-1.15} \pm 0.61$	$1.60^{+1.91}_{-1.06} \pm 0.08$	$2.12^{+2.38}_{-1.65} \pm 0.17$	553.347	0.3677	0.57	0.00	19	1333.0
G067.52+34.75	NFW	pHer	$2.03^{+0.44}_{-0.39} \pm 0.05$	$1.96^{+0.68}_{-0.62} \pm 0.34$	$1.27^{+1.87}_{-1.24} \pm 0.61$	$1.54^{+1.90}_{-1.06} \pm 0.08$	$1.63^{+2.34}_{-1.19} \pm 0.17$	940.716	0.1822	0.41	0.17	116	952.6
G113.29-29.69	NFW	pNFW	$1.86^{+0.30}_{-0.28} \pm 0.05$	$0.41^{+0.15}_{-0.16} \pm 0.34$	$0.42^{+0.83}_{-0.41} \pm 0.61$	$1.57^{+1.81}_{-1.06} \pm 0.08$	$1.84^{+2.42}_{-1.39} \pm 0.17$	958.728	0.103	0.45	0.14	114	907.7
G192.18+56.12	Bur	pHer	$1.66^{+0.79}_{-1.06} \pm 0.05$	$2.20^{+0.63}_{-0.73} \pm 0.34$	$1.72^{+1.65}_{-1.35} \pm 0.61$	$1.35^{+2.00}_{-0.88} \pm 0.08$	$1.42^{+2.25}_{-0.98} \pm 0.17$	834.688	0.1268	0.70	0.25	104	844.6

PSZ2 name	Mass	$N(R)$	$r_{200}$ [Mpc]	$r_v$ [Mpc]	$r_s$ [Mpc]	$\mathcal{A}_\infty$	$\mathcal{A}_\infty$	$-\ln P$	$z$	$A^2$	$f_{\text{sub}}$	$N_{200}$	$\sigma_{\text{ap},200}$ [km/s]
G179.09+60.12	Bur	pNFW	$2.53^{+0.93}_{-1.26}$	$0.67^{+0.40}_{-0.30}$	$1.00^{+1.96}_{-0.99}$	$1.57^{+1.92}_{-1.10} \pm 0.08$	$2.11^{+2.30}_{-1.63} \pm 0.17$	808.742	0.1397	0.14	0.12	76	1195.0
G283.91+73.87	Bur	pHer	$1.79^{+0.58}_{-0.83}$	$1.46^{+0.65}_{-0.42}$	$0.77^{+1.66}_{-0.77} \pm 0.15$	$1.56^{+1.89}_{-1.09} \pm 0.09$	$1.80^{+2.37}_{-1.35} \pm 0.10$	671.203	0.08635	0.30	0.28	88	806.1
G149.39-36.84	Eis	pHer	$1.65^{+0.53}_{-0.66}$	$3.15^{+1.49}_{-1.32} \pm 0.14$	$1.42^{+1.99}_{-1.40} \pm 0.15$	$1.46^{+1.94}_{-1.00} \pm 0.09$	$2.12^{+2.35}_{-1.63} \pm 0.10$	657.580	0.1699	0.44	0.19	100	865.8
G040.03+74.95	NFW	pHer	$4.26^{+0.65}_{-0.64}$	$1.64^{+0.38}_{-0.23} \pm 0.14$	$0.96^{+1.28}_{-0.86} \pm 0.15$	$1.49^{+1.76}_{-0.95} \pm 0.09$	$1.67^{+2.36}_{-1.23} \pm 0.10$	1645.232	0.07067	4.63	0.39	241	2084.0
G040.03+74.95a	NFW	pHer	$2.76^{+0.49}_{-0.45}$	$1.42^{+0.41}_{-0.37} \pm 0.29$	$1.31^{+1.89}_{-1.21} \pm 0.60$	$1.61^{+2.65}_{-1.15} \pm 0.11$	$1.50^{+2.58}_{-1.05} \pm 0.08$	1186.989	0.07558	0.54	0.24	125	1180.0
G217.09+40.15	NFW	pHer	$1.83^{+0.35}_{-0.32}$	$1.47^{+0.49}_{-0.39} \pm 0.14$	$1.09^{+1.98}_{-1.09} \pm 0.15$	$1.40^{+1.73}_{-0.94} \pm 0.09$	$2.11^{+2.35}_{-1.61} \pm 0.10$	1050.259	0.1382	1.42	0.33	117	884.8
G172.74+65.30	NFW	pNFW	$1.57^{+0.47}_{-0.42}$	$0.52^{+0.32}_{-0.19} \pm 0.14$	$1.25^{+1.96}_{-1.24} \pm 0.15$	$1.28^{+1.83}_{-0.83} \pm 0.09$	$2.05^{+2.34}_{-1.57} \pm 0.10$	577.073	0.07529	0.30	0.20	74	720.3
G105.55+77.21	NFW	pHer	$1.72^{+0.41}_{-0.36}$	$1.34^{+0.58}_{-0.42} \pm 0.14$	$1.33^{+1.97}_{-1.32} \pm 0.15$	$1.31^{+1.87}_{-0.85} \pm 0.09$	$1.98^{+2.45}_{-1.51} \pm 0.10$	700.214	0.07242	0.36	0.17	85	743.2
G066.68+68.44	Bur	pHer	$1.64^{+0.35}_{-0.29}$	$1.63^{+0.63}_{-0.53} \pm 0.14$	$0.36^{+0.73}_{-0.34} \pm 0.15$	$1.79^{+1.82}_{-1.24} \pm 0.09$	$1.77^{+2.41}_{-1.32} \pm 0.10$	845.978	0.1625	0.15	0.11	97	834.4
G050.40+31.17	NFW	pNFW	$1.89^{+0.46}_{-0.43}$	$0.63^{+0.37}_{-0.24} \pm 0.52$	$1.18^{+1.83}_{-1.14} \pm 0.46$	$1.33^{+1.92}_{-0.87} \pm 0.08$	$1.69^{+2.27}_{-1.25} \pm 0.16$	837.047	0.1605	0.36	0.07	95	922.0
G057.78+52.32	Eis	pHer	$1.65^{+0.29}_{-0.27}$	$0.94^{+0.29}_{-0.25} \pm 0.52$	$0.32^{+0.55}_{-0.30} \pm 0.46$	$1.79^{+1.83}_{-1.25} \pm 0.08$	$2.01^{+2.39}_{-1.55} \pm 0.16$	848.210	0.06628	0.23	0.14	104	793.8
G040.58+77.12	NFW	pHer	$1.43^{+0.48}_{-0.51}$	$2.52^{+1.64}_{-1.12} \pm 0.52$	$1.58^{+1.92}_{-1.54} \pm 0.46$	$1.21^{+1.77}_{-0.75} \pm 0.08$	$2.20^{+2.32}_{-1.64} \pm 0.16$	442.840	0.0754	0.34	0.00	60	652.6
G028.63+50.15	Her	pHer	$1.84^{+0.49}_{-0.44}$	$0.73^{+0.36}_{-0.31} \pm 0.52$	$1.55^{+1.90}_{-1.49} \pm 0.46$	$1.43^{+1.94}_{-0.97} \pm 0.08$	$1.95^{+2.45}_{-1.49} \pm 0.16$	416.306	0.09083	0.32	0.06	50	789.6
G186.37+37.26	Bur	pNFW	$2.25^{+0.28}_{-0.26}$	$0.87^{+0.24}_{-0.14} \pm 0.14$	$0.36^{+0.38}_{-0.28} \pm 0.69$	$1.79^{+1.78}_{-1.17} \pm 0.11$	$1.32^{+2.12}_{-0.87} \pm 0.09$	2213.302	0.2818	0.48	0.21	243	1240.0
G228.16+75.20	Bur	pHer	$2.54^{+0.34}_{-0.31}$	$0.75^{+0.09}_{-0.11} \pm 0.14$	$0.29^{+0.24}_{-0.19} \pm 0.69$	$1.93^{+1.79}_{-1.42} \pm 0.11$	$0.95^{+1.17}_{-0.48} \pm 0.09$	2705.849	0.5423	0.72	0.31	293	1512.0
G286.98+32.90	Her	pNFW	$3.21^{+0.77}_{-0.70}$	$0.31^{+0.23}_{-0.18} \pm 0.14$	$1.24^{+1.88}_{-1.22} \pm 0.69$	$1.59^{+1.92}_{-1.12} \pm 0.11$	$1.95^{+2.41}_{-1.50} \pm 0.09$	619.176	0.386	0.16	0.00	73	1816.0
G028.89+60.13	Her	pNFW	$1.70^{+0.32}_{-0.30}$	$0.60^{+0.30}_{-0.23} \pm 0.14$	$1.35^{+1.85}_{-1.22} \pm 0.69$	$1.46^{+1.87}_{-1.00} \pm 0.11$	$1.82^{+2.49}_{-1.37} \pm 0.09$	1001.433	0.1519	0.19	0.09	120	817.2
G087.03-57.37	Bur	pNFW	$1.86^{+0.69}_{-1.22}$	$0.72^{+0.39}_{-0.30} \pm 0.50$	$1.28^{+1.53}_{-1.12} \pm 0.73$	$1.43^{+1.87}_{-0.97} \pm 0.09$	$2.08^{+2.29}_{-1.58} \pm 0.10$	1085.206	0.2761	0.33	0.32	97	1002.0
G071.63+29.78	Bur	pHer	$1.82^{+0.89}_{-1.12}$	$1.50^{+0.49}_{-0.49} \pm 0.50$	$1.97^{+1.63}_{-1.46} \pm 0.73$	$1.22^{+1.95}_{-0.76} \pm 0.09$	$1.88^{+2.35}_{-1.34} \pm 0.10$	807.446	0.1575	0.41	0.33	91	844.3
G073.97-27.82	NFW	pNFW	$2.48^{+0.23}_{-0.22}$	$0.72^{+0.20}_{-0.17} \pm 0.50$	$0.46^{+0.46}_{-0.34} \pm 0.73$	$1.95^{+1.68}_{-1.19} \pm 0.09$	$1.04^{+1.37}_{-0.58} \pm 0.10$	3368.643	0.2282	0.74	0.34	353	1315.0
G092.71+73.46	NFW	pHer	$2.74^{+0.39}_{-0.36}$	$1.95^{+0.37}_{-0.40} \pm 0.50$	$1.16^{+1.64}_{-1.04} \pm 0.73$	$1.50^{+1.85}_{-0.97} \pm 0.09$	$1.69^{+2.39}_{-1.23} \pm 0.10$	2246.441	0.2317	0.97	0.18	261	1407.0



PSZ2 name	Mass	$N(R)$	$r_{200}$ [Mpc]	$r_v$ [Mpc]	$r_s$ [Mpc]	$\mathcal{A}_\infty$	$\mathcal{A}_0$	$-\ln P$	$z$	$A^2$	$f_{\text{sub}}$	$N_{200}$	$\sigma_{\text{ap},200}$ [km/s]
G187.53+21.92	Bur	pNFW	$1.63^{+0.33}_{-0.29} \pm 0.06$	$0.71^{+0.31}_{-0.23} \pm 0.50$	$0.37^{+0.38}_{-0.34} \pm 0.73$	$1.59^{+1.86}_{-1.11} \pm 0.09$	$1.65^{+2.55}_{-1.19} \pm 0.10$	1407.205	0.1707	0.53	0.24	168	846.2
G278.58+39.16	NFW	pHer	$2.18^{+0.34}_{-0.32} \pm 0.06$	$1.75^{+0.35}_{-0.42} \pm 0.50$	$0.81^{+1.74}_{-0.81} \pm 0.73$	$1.62^{+1.78}_{-1.10} \pm 0.09$	$1.95^{+2.39}_{-1.50} \pm 0.10$	1170.971	0.3063	0.24	0.26	130	1164.0
G218.81+35.51	Bur	pHer	$3.70^{+0.57}_{-0.61} \pm 0.06$	$2.24^{+0.38}_{-0.37} \pm 0.50$	$1.85^{+1.86}_{-1.88} \pm 0.73$	$2.50^{+1.54}_{-2.03} \pm 0.09$	$3.63^{+1.50}_{-2.20} \pm 0.10$	4820.696	0.1663	22.14	0.32	486	1852.0
G218.81+35.51 a	Eis	pHer	$1.03^{+0.42}_{-0.48} \pm 0.06$	$3.42^{+0.36}_{-0.55} \pm 0.40$	$1.46^{+1.92}_{-1.37} \pm 0.65$	$1.87^{+2.62}_{-1.39} \pm 0.11$	$2.09^{+2.55}_{-1.59} \pm 0.10$	1357.077	0.1643	0.9179	0.35	151	671.7
G218.81+35.51 b	Bur	pNFW	$1.52^{+0.46}_{-0.43} \pm 0.07$	$0.62^{+0.23}_{-0.25} \pm 0.22$	$0.49^{+0.80}_{-0.44} \pm 0.72$	$2.08^{+2.61}_{-1.61} \pm 0.09$	$1.36^{+2.71}_{-0.90} \pm 0.09$	843.035	0.1776	0.70	0.32	89	769.0
G049.32+44.37	NFW	pHer	$1.74^{+0.38}_{-0.37} \pm 0.06$	$1.57^{+0.56}_{-0.40} \pm 0.50$	$1.71^{+1.83}_{-1.51} \pm 0.73$	$1.27^{+1.84}_{-0.81} \pm 0.09$	$1.94^{+2.46}_{-1.44} \pm 0.10$	1124.578	0.09606	0.20	0.24	134	763.8
G046.10+27.18	Her	pHer	$3.29^{+0.96}_{-0.92} \pm 0.06$	$0.57^{+0.29}_{-0.23} \pm 0.50$	$1.96^{+1.72}_{-1.48} \pm 0.73$	$1.28^{+1.93}_{-0.81} \pm 0.09$	$1.69^{+2.54}_{-1.24} \pm 0.10$	560.821	0.3878	0.57	0.05	63	1598.0
G262.73-40.92	NFW	pHer	$2.79^{+0.96}_{-0.86} \pm 0.06$	$0.59^{+0.22}_{-0.23} \pm 0.50$	$1.39^{+1.92}_{-1.34} \pm 0.73$	$1.24^{+2.06}_{-0.78} \pm 0.09$	$1.98^{+2.39}_{-1.48} \pm 0.10$	530.355	0.4218	0.44	0.18	67	1281.0
G206.45+13.89	Bur	pHer	$3.54^{+1.10}_{-0.91} \pm 0.06$	$0.98^{+0.47}_{-0.39} \pm 0.50$	$1.12^{+1.57}_{-0.97} \pm 0.73$	$1.51^{+1.96}_{-1.06} \pm 0.09$	$1.35^{+2.37}_{-0.90} \pm 0.10$	553.161	0.4054	0.37	0.07	59	1496.0
G083.29-31.03	NFW	pHer	$2.44^{+0.64}_{-0.57} \pm 0.20$	$0.74^{+0.14}_{-0.18} \pm 0.27$	$1.56^{+1.90}_{-1.48} \pm 0.51$	$1.32^{+1.90}_{-0.86} \pm 0.14$	$1.86^{+2.42}_{-1.40} \pm 0.19$	546.380	0.4102	0.40	0.00	21	1106.0
G201.50-27.31	NFW	pHer	$2.35^{+0.31}_{-0.29} \pm 0.06$	$1.31^{+0.31}_{-0.25} \pm 0.50$	$1.13^{+1.55}_{-0.98} \pm 0.73$	$1.44^{+1.72}_{-0.90} \pm 0.09$	$1.65^{+2.37}_{-1.19} \pm 0.10$	2281.875	0.539	0.93	0.31	241	1346.0
G057.25-45.34	Bur	pHer	$2.52^{+1.04}_{-1.77} \pm 0.14$	$4.72^{+3.45}_{-2.61} \pm 1.22$	$1.15^{+2.19}_{-1.14} \pm 0.20$	$1.65^{+1.86}_{-1.19} \pm 0.08$	$1.96^{+2.45}_{-1.50} \pm 0.06$	479.187	0.3977	0.41	0.21	54	1591.0
G111.61-45.71	Her	pHer	$2.66^{+0.45}_{-0.42} \pm 0.06$	$0.98^{+0.21}_{-0.16} \pm 0.50$	$1.40^{+1.66}_{-1.16} \pm 0.73$	$1.37^{+1.97}_{-0.91} \pm 0.09$	$1.54^{+2.45}_{-1.10} \pm 0.10$	2157.449	0.5477	0.76	0.23	255	1866.0

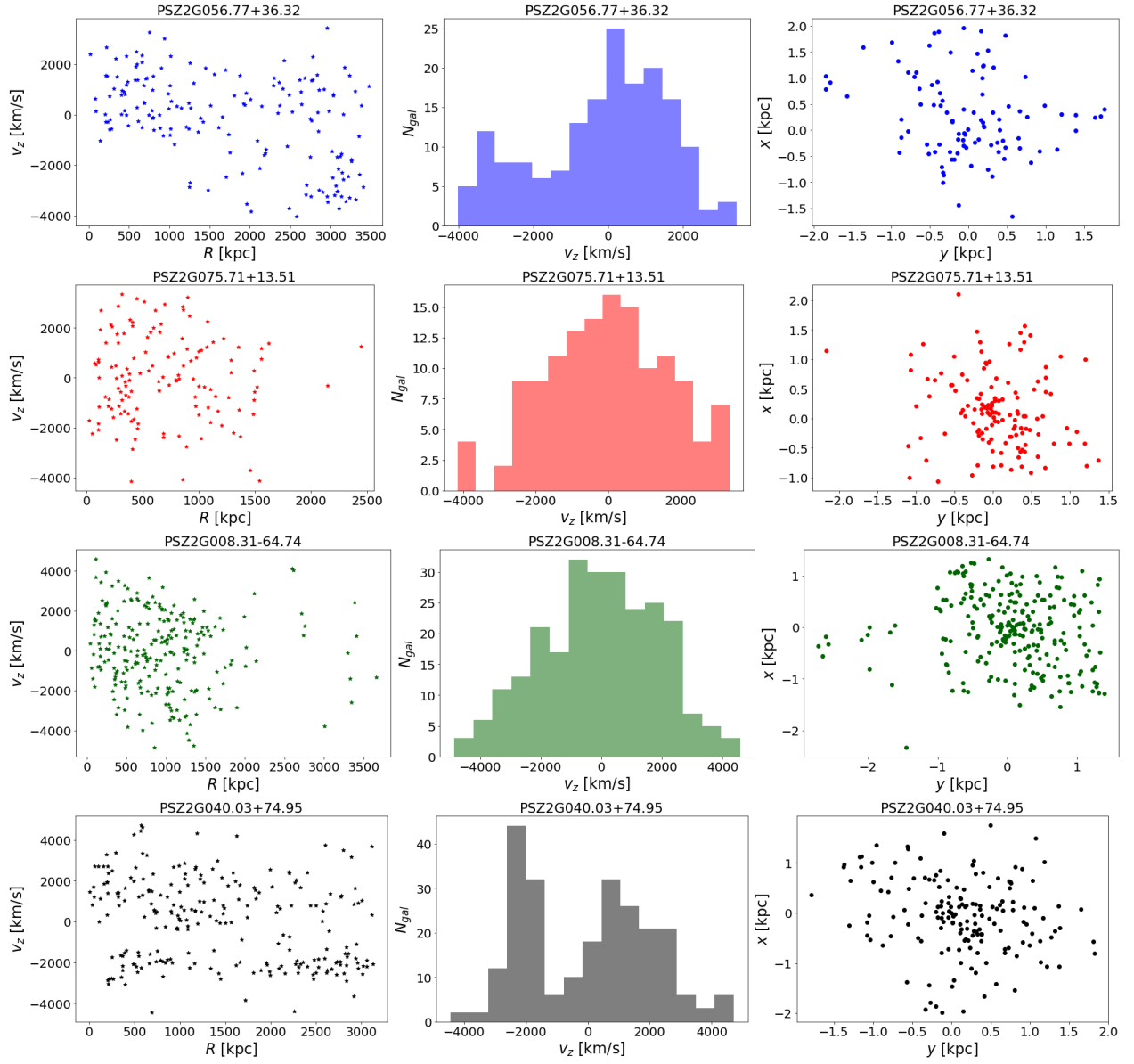


**Fig. B.1.** Each row represent one of the four clusters in the sample showing a logarithmic scatter  $\delta\eta > 0.8$  dex. Left: projected phase space. Central: LOS velocity distribution. Right: projected positions with respect to the cluster center.

**Table D.1.** Extract of the galaxies with measured spectroscopic redshift in the field of PSZ2G083.29-31.03.

ID	RA (deg ; J2000)	Dec	$z$	$\delta z$
1	337.14050	20.62120	0.41158	0.00009
2	337.13602	20.62673	0.42092	0.00013
3	337.15583	20.61639	0.40267	0.00013
4	337.13124	20.59847	0.41477	0.00013
5	337.15079	20.59610	0.42112	0.00009
6	337.11054	20.61091	0.41220	0.00011
7	337.10786	20.61638	0.41187	0.00008
8	337.13583	20.59031	0.41003	0.00008
9	337.17094	20.63067	0.41885	0.00013
10	337.17612	20.60638	0.41726	0.00010

**Table D.2.** Extract of the galaxies with measured spectroscopic redshift in the field of PSZ2G113.91-37.01.

ID	RA (deg ; J2000)	Dec	$z$	$\delta z$
1	4.92222	25.30204	0.36999	0.00007
2	4.93030	25.30678	0.35787	0.00006
3	4.93419	25.28389	0.36852	0.00009
4	4.93971	25.31805	0.36313	0.00012
5	4.90339	25.31256	0.36536	0.00008
6	4.95634	25.30796	0.37480	0.00008
7	4.90230	25.27815	0.36741	0.00009
8	4.88488	25.28588	0.35860	0.00012
9	4.90188	25.34320	0.37568	0.00008
10	4.91762	25.25141	0.36569	0.00009

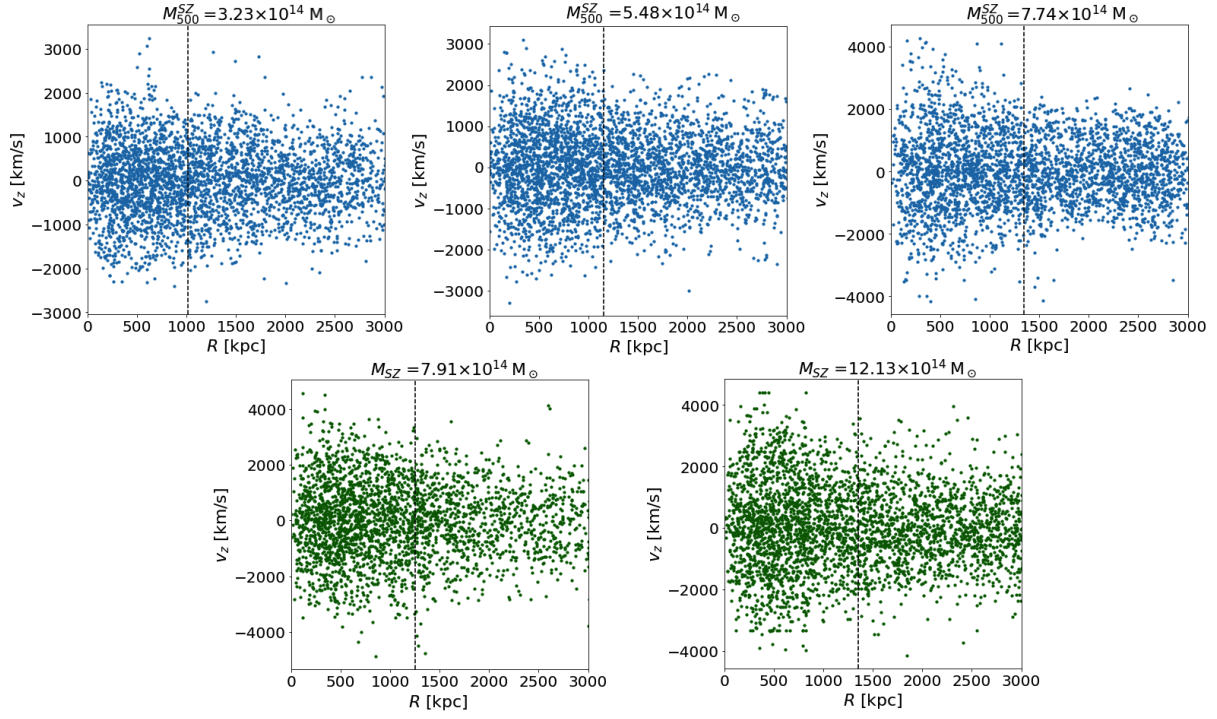


**Fig. C.1.** The projected phase space (PPS) parameters (radius  $R$  and radial velocity  $v$ ) for the SZ-stacked clusters. Top, blue points: Tier 1. Bottom, green points: Tier 2. The vertical dashed lines indicate the average  $r_{500}$  of all the clusters in each stacking.

**Table D.3.** Extract of the galaxies with measured spectroscopic redshift in the field of PSZ2G046.10+27.18.

ID	RA (deg ; J2000)	Dec	z	$\delta z$
1	262.93623	22.80826	0.38764	0.00037
2	262.90941	22.81799	0.38311	0.00014
3	262.91685	22.81963	0.37632	0.00010
4	262.92559	22.82227	0.39349	0.00021
5	262.90121	22.82538	0.37398	0.00027
6	262.90976	22.82926	0.37562	0.00017
7	262.90436	22.83141	0.38326	0.00014
8	262.89507	22.83543	0.38148	0.00020
9	262.93955	22.83818	0.37660	0.00033
10	262.89412	22.83914	0.38374	0.00033